FABRICATION OF NANOCOMPOSITE USING ONE POT HYDROTHERMAL TREATMENT AND APPLICATION THEREOF

A thesis submitted in the fulfillment of the requirements for the award of the degree of

Master of Engineering

From

Jadavpur UniversityKolkata

Submitted by

Huzaifa Masud Mondal

Exam Roll No: M4CHE24020

Class Roll No: 002210302020

Registration No: 135725 OF 2016-17

under the supervision of

Dr. Sudeshna Saha

Department of Chemical Engineering

Jadavpur University

Kolkata 700032

West Bengal, India

CERTIFICATE

To whom it may concern

This is to certify that the project entitled **"Fabrication of nanocomposite using one pot hydrothermal treatment and application thereof"** is hereby approved as a creditable study in the area of **Chemical Engineering** carried out satisfactorily by **Huzaifa Masud Mondal** (University Exam Roll No: **M4CHE24020** , Registration No: **135725 of 2016-17** , Class Roll No: **002210302020**) to warrantit's acceptance as a partial pre-requisite for the award for the degree of **Master of Chemical Engineering** from **Jadavpur University, Kolkata**. It is understood that by this approval the undersigned do not necessarily endorse or approve any statement made, opinion expressed or conclusion drawn therein, but approve the project only for the purpose for which it is submitted. The contents embodied in this thesis have not been submitted to any other University for the award of any degree or diploma.

Sudeshna Saha 30/7/24

Dr. Sudeshna Saha

(Thesis Supervisor)

Assistant Professor

Dept. of Chemical Engineering

Jadavpur University

Assistant Professor
CHEMICAL ENGINEERING DEPARTMENT
JADAVPUR UNIVERSITY
Kolkata-700 032

P Das 30/07/24

Dr. Papita Das

Professor & Head

Dept. of Chemical Engineering

Jadavpur University

HEAD
CHEMICAL ENGINEERING DEPARTMENT
JADAVPUR UNIVERSITY
Kolkata-700 032

Dipak Laha 30/7/24

Prof. Dipak Laha

Dean, Faculty of Engg. & Tech.

Jadavpur University

DEAN
Faculty of Engineering & Technology
JADAVPUR UNIVERSITY
KOLKATA-700 032

DECLARATION

This declaration is to certify that the work presented in this thesis was completed by the author, unless specified otherwise, and that no part of it has been submitted in a thesis to any other university or institution.

This thesis was prepared in a compilation style format and is based on the experiments performed in the Energy Lab, Department of Chemical Engineering, Jadavpur University. All the related experiments were conducted and written during the author's candidature enrolled in M.E. Chemical Engineering (2022- 2024).

Despite a certain level of repetition between chapters and introductory material and analytic methods, each single chapter was substantially different in focus and content within the scope of the thesis theme.

Huzaifa Masud Mondal

Huzaifa Masud Mondal

July 2024

Kolkata

ACKNOWLEDGEMENT

I would firstly like to thank my supervisor Dr. Sudeshna Saha (Department of Chemical Engineering, Jadavpur University) whose input proved invaluable throughout my Master's thesis.

I would also like to thank my department head Prof. Papita Das to have given me this wonderful opportunity to work on this project in the department of Chemical engineering, Jadavpur University.

I would like to thank Dr. Sujata Sardar (Assistant Professor, Jadavpur University) who also guided me throughout my Master's thesis.

I would like to thank Saswata Chakrabarty (PhD Scholar) who also helped me throughout my research work.

Finally, I would like to thank my lab partner Avra Mondal, Yamini Mishra and Mousom Roy for their help and co-operation.

Special thanks must go to the technical staffs, past and present, at the University,and my friend Suroj Ikbal for his support throughout my Master Degree.

Thanking you,

Huzaifa Masud Mondal

Exam Roll Number: M4CHE24020

Class Roll Number: 0022103020

Registration Number: 135725 of 2016-17

M.E. 2nd Year

Contents

1. Introduction 1
1.1 Nanoscience and Nanotechnology: 1
1.2 Why Nanotechnology? 2
1.3 The Evolution of Nanotechnology and Its History: 3
1.4 Grouping of nanomaterials 5
1.4.1 Zero-dimensional materials (0-D) 6
1.4.2 One-dimensional materials (1-D) 6
1.4.3 Two-dimensional materials (2-D) 6
1.5 Optical and Electrical properties of nanomaterials 7
1.5.1 Transmittance and Absorption 7
1.5.2 Electrical conductivity 7
1.7 Dye Removal from Wastewater 9
1.8 What is MoS_2? 10
1.8.1 Structure and polymorphs 11
1.8.2 Application of MoS_2 12
1.8.3 Different synthesis methods of MoS_2: 13
2 LITERATURE REVIEW 16
2.1 Literature review on the synthesis of MoS_2 nanomaterial 16
2.2 Literature review on applications of MoS_2 nanomaterial 18
2.2.1 Hydrogen Evolution 18
2.2.2 Enhanced Energy Storage Capability 19
2.2.3 Electromagnetic Wave Absorption Property 20
2.2.4 Multiple Wavelength Optical Sensing Applications 21
2.2.5 Thermal Battery 21
2.2.6 Visible Light Photocatalytic Degradation of Dyes 22
2.3 Literature review on the synthesis of MoS_2 nanocomposites 25
2.3.1 Room temperature humidity sensors based on rGO/MoS_2 hybrid composites synthesized by hydrothermal method 25
2.3.2 One-step hydrothermal synthesis of a CoS_2@MoS_2 nanocomposite for high-performance supercapacitors 26
2.3.3 Synthesis of unique-morphological hollow microspheres of MoS_2@montmorillonite nanosheets for the enhancement of photocatalytic activity and cycle stability 27
2.3.4 Facile synthesis of MoS_2 nanoflower-Ag NPs grown on lignin-derived graphene for Troponin I aptasensing 28

2.3.5 MoS_2/RGO hybrids prepared by a hydrothermal route as a highly efficient catalytic for sonocatalytic degradation of methylene blue 30
2.3.6 Clean energy by using $NiCo_2O_4$/MoS_2 nanocomposites prepared by hydrothermal method 31
2.3.7 Hydrothermal Synthesis and Electrochemical Properties of MoS_2/C Nanocomposite 32
2.3.8 MoS_2−Ag Nanocomposite-Based SERS Substrates with an Ultralow Detection Limit 33
2.3.9 Characterizations of synthesized laser-scribed graphene/ molybdenum disulfide (LSG/MoS_2) hybrids for supercapacitor performance 34
2.3.10 Hydrothermal Synthesis of MoS_2/SnS_2 Photocatalysts with Heterogeneous Structures Enhances Photocatalytic Activity 35
2.3.11 Fe_3O_4@MoS_2/RGO as an effective nano-electrocatalyst toward electrochemical hydrogen evolution reaction and methanol oxidation in two settings for fuel cell application 36
2.4 Literature review on Dye degradation 37
2.4.1 Sunlight-driven MoS_2 nanosheets mediated dye degradation 37
2.4.2 Degradation of mixed dye pollutants by integrated adsorption-photocatalysis technique 38
2.4.3 Rapid degradation of Rhodamine B under concentrated sunlight irradiation 38
2.4.4 Layered MoS_2 for photocatalytic dye degradation 39
2.4.5 Photocatalytic Degradation of Methyl Orange using MoS_2 nanoparticles as catalyst 39
2.4.6 Green synthesis of MoS_2 for degrading MB and CV under natural sunlight 40
2.4.7 Photocatalytic Dye Degradation by MoS2 NS synthesized by different routes 40
2.4.8 Sodium dodecyl sulfate mediated hydrothermal synthesis of MoS_2 NSs 41
2.5 Objectives 42
3 Experimental Methods 43
3.1 Experimental Design 43
3.2 Materials & Methods 43
3.3 Hydrothermal synthesis of MoS_2 nanomaterials 44
3.4 Dye Degradation Experiments 45
3.5 Characterizations of prepared Nanomaterials 46
4 INSTRUMENTS AND APPARATUS 46
4.1 UV-Vis Diffuse Reflectance Spectroscopy 46
4.2 Ultraviolet-Visible Spectrophotometer 48
4.3 Dynamic Light Scattering and Zeta-Potential Measurement 49

4.3.1 Dynamic Light Scattering (DLS) 49
4.3.2 Zeta potential 50
4.4 Fourier Transform Infrared (FTIR) Spectroscopy 51
5 Results & Discussion 53
5.1 Photocatalytic performance of prepared MoS_2 samples in dye degradation 53
5.1.1 Effect of synthesis parameters and additional chemicals used on the degradation performance of synthesized MoS_2 53
5.1.2 Effect of varying pH on the degradation performance of synthesized MoS_2 54
5.1.3 Effect of catalyst loading on the degradation performance of synthesized MoS_2 56
5.1.4 Effect of dye concentration on the dye degradation performance of synthesized MoS_2 57
5.1.5 Kinetics of Photocatalytic dye degradation by synthesized MoS_2 58
5.2 Characterization of prepared MoS_2 samples 60
5.2.1 UV-Vis Diffuse Reflectance Spectroscopy 60
5.2.2 Particle size & Zeta potential analysis 61
5.2.3 FTIR Analysis 66
6 Conclusion 68
7 References 70

List of Figures

Figure 1: Different Structures of MoS_2 11
Figure 2: Experimental Design 43
Figure 3: Preparation of MoS_2 44
Figure 4: UV-Vis Spectrophotometer (Perkin Elmer UV-Vis Lambda 365) 49
Figure 5: DLS Zeta-potential instrument (Malvern Zetasizer) 50
Figure 6: FTIR (Jasco FT/IR-4700) 52
Figure 7: Effect of synthesis parameters and additional chemicals used on the degradation performance of synthesized MoS_2 towards 50ppm MG under sunlight 53
Figure 8: Degradation of malachite green dye at, (a) pH 2, (b) pH 4 and (c) neutral pH 55
Figure 9: Dye degradation at varying catalyst loading at, (a) 50 ppm, and (b) 300 ppm malachite green concentration 56
Figure 10: Effect of dye concentration and contact time on the dye degradation performance of synthesized MoS_2 57
Figure 11: Kinetics of Photocatalytic dye degradation by synthesized MoS_2 59
Figure 12: Tauc's plot for synthesized MoS_2 samples 61
Figure 13: Particle size analysis of MoS_2 samples selected for dye degradation experiments 61
Figure 14: Zeta potential and Isoelectric points of investigated MoS_2 samples 65
Figure 15: FTIR spectra of MoS_2 samples under investigation 66

List of Tables

Table 1: Changes of properties at the nano-size scale for various materials 2
Table 2: Methods of synthesis of MoS_2: 14
Table 3: Synthesis of MoS_2 nano-composites 23
Table 4: MoS_2 samples prepared under varying conditions 45
Table 5: pH values at which the samples in suspension display their isoelectric point 65

1. Introduction

1.1 Nanoscience and Nanotechnology:

Nanoscience and technology encompass the study and application of materials and systems at the nanometer scale, which is one billionth of a meter. This scale is roughly equivalent to the size of an atom or a small molecule. At this incredibly small scale, materials exhibit unique and distinct properties vastly different from those observed at the macroscale. These novel characteristics have led to the rapid growth and interdisciplinary nature of nanoscience and technology, as researchers and scientists explore new possibilities and applications across various fields.

Nanoscience and technology hold significant promise across various fields, including medicine, electronics, energy, and materials science. In medicine, researchers are exploring the use of nanoparticles for targeted drug delivery to specific cells within the human body. In electronics, advancements are being made with semiconductor nanowires, which are considered components for computer chips, enabling the creation of tiny transistors. In the energy sector, nanomaterials such as carbon nanotubes are being investigated to improve the efficiency of solar cells and batteries. Additionally, in materials science, the development of nanocomposites with enhanced strength and durability is underway [1,5].

Nanoscience and technology are driving the creation of innovative materials with unique properties, leading to advancements in various applications. These include the development of new catalysts for chemical reactions, sophisticated drug delivery systems for precise medical treatments, advanced imaging and diagnostic tools for better disease detection, and numerous other cutting-edge applications.

Nanoscience and technology hold immense potential in the field of medicine. Nanoparticles can be meticulously engineered to deliver drugs specifically to cancer cells, minimizing side effects and improving the effectiveness of treatments. Additionally, nanoparticles offer the potential to create diagnostic tools capable of detecting diseases at an early stage.

In the realm of electronics, nanoscience and technology are poised to bring about a revolution. Nanomaterials like carbon nanotubes and graphene exhibit unique electrical properties that could significantly enhance the speed and efficiency of computer processors. Moreover, nanoscale transistors could lead to the development of electronic devices that consume much less power, paving the way for more energy-efficient gadgets [7-9].

While nanoscience and technology offer numerous promising benefits, there are also concerns about their potential risks. Some studies suggest that exposure to nanoparticles could lead to negative health effects, while other research raises questions about the environmental impact of nanomaterials. Therefore, it is crucial to continue conducting thorough investigations into both the potential hazards and benefits of nanoscience and technology. This ongoing research will help ensure the development of safe and effective applications in this rapidly evolving field [5].

Although nanoscience and technology present a wealth of promising benefits, there are also significant concerns regarding their potential risks. Some research indicates that exposure to nanoparticles could result in adverse health effects, while other studies highlight the potential environmental impacts of nanomaterials. Consequently, it is essential to persist in conducting comprehensive investigations into both the hazards and advantages of nanoscience and technology. Such ongoing research is vital to ensure the safe and effective development and application of these advancements in this rapidly evolving field. [8].

1.2 Why Nanotechnology?

The meticulous and regulated production of innovative materials and devices with unique properties by assembling or constructing atoms and molecules at the nanoscale (10^{-9} m) level. Understanding, modifying, and using matter at the nanoscale, where materials' characteristics differ from those of their bulk counterparts, is the focus of nanotechnology. Scientists may provide novel solutions in a variety of sectors, such as electronics, materials science, health, energy, and environmental research, by designing and manipulating nanoscale structures and devices. It provides previously unheard-of control over the fundamental components of matter, opening the door to the development of innovative materials, sensors, tools, and systems with improved functionality and performance [10]. The electron transfer properties of macro-sized and nano-sized particles of the same materials are different.

Table 1: Changes of properties at the nano-size scale for various materials

MATERIALS	MACRO-SIZE	NANO-SIZE
Lead sulphide	Is an insulator	Becomes conductor
Iron oxide	The band gap is 1.95 eV	The band gap is 3.1 eV
Carbon	Electron emission at 2500 V	Electron emission at a much lower voltage of 2.5 V

1.3 The Evolution of Nanotechnology and Its History:

Nanotechnology may be a recent field of study, but research on the nanoscale scale is not. The nanometer regime has long been used in the study of biological systems and the production of metal-based products including metallic quantum dots, colloidal dispersions, and catalysts. A historical analysis reveals that nanotechnology has existed since the dawn of human culture. Early examples of nanostructured materials were based on the empirical knowledge of craftsmen and their early material manipulation [11]. The most significant scientific breakthroughs in nanotechnology, with direct applications and implications, have arisen in the modern era due to the invention and remarkable advancement of spectroscopic and characterization instruments, such as Transmission Electron Microscopy and Field Emission Scanning Electron Microscopy, among others.

4th century: Glass colored by Ag and Au nanoparticles (Lycurgus cup, British Museum).

9th to 17th century: Glowing, glittering "luster" glazes.

About 2000 years ago: In ancient Egypt, common men used nanoparticles called galenite (lead sulfide), a dying paste to their hair black, a few nanometres in size. They were able to make this by reacting lime, lead oxide, and a small amount of water. More than 1000 years ago: the Chinese are known to use Au nanoparticles as an inorganic dye to introduce red color into their ceramic porcelains.

19th century: Photography using Ag nanoparticles.

1857: Colloidal dispersion of gold (Au) prepared by Michael Faraday.

1931: The first Transmission Electron Microscope was built by Max Knoll and Ernst Ruska in 1931, with this group developing the first TEM with a resolution greater than that of light in 1933 and the first commercial TEM in 1939. In 1986, Ruska was awarded the Nobel Prize in Physics for the development of Transmission Electron Microscopy.

1936: Erwin Muller invented the field emission Microscope.

1950: Victor La Mer and Robert Dinegar developed the theory and a process for growing monodisperse Colloids.

1956: Arthur von Hippel introduced "molecular engineering ".

1958: Jack Kilby built the first integrated circuit.

1959: Richard Feynman projected engineering at the atomic scale.

1965: Moore's Law.

1972: Field Emission Scanning Electron Microscope was invented by Albert with the help of Hitachi

1974: Professor Norio Taniguchi at the University of Tokyo first invented the term "nanotechnology".

1981: Gerd Binning and Heinrich Rohrer invented the Scanning Tunnelling Microscope. They awarded the Nobel Prize in Physics in 1986.

1985: Discovery of Buckminsterfullerene (C60) at Rice University by Richard Smalley, Robert Curl, James Heath, Sean O'Brien, and Harold Kroto.

1986: Gerd Binning, Calvin Quate, and Christoph Gerber invented the atomic force Microscope.

1991: The carbon nanotube was discovered by Prof. Sumio Iijima.

1992: C.T. Kresge and colleagues discovered the nanostructured MCM-41 and MCM-48.

1993: Invention of controlled synthesis of nanocrystals.

1998: Dr. Nadrian, C. Seeman, and his co-workers at New York University announced in January a major advance along one potential path toward molecular nanotechnology that involves making devices from branched DNA molecules.

1999: Dip pin nanolithography was invented by the Mirkin Group.

2003: 21st century Nanotechnology Research Report.

2005: DNA-based computer and "algorithmic self-assembly".

2007: Lithium-ion battery with a common type of virus.

2009: Several DNA-like robotic Nanoscale assembly devices.

2010: Graphene, two dimensional, one of the allotropes of carbon was discovered in 2004 by Ande Geim and Konstantin Novoselov at the University of Manchester and they were awarded Nobel Prize in physics in 2010.

2014: The NNI release the updated 2014 Strategic Plan.

1.4 Grouping of nanomaterials

The previous several decades have seen a rapid expansion of the domains of nanoscience and nanotechnology due to the discovery of innovative synthesis pathways, characterization techniques, and manipulation tools. Among the numerous varieties of nanoscale structures are thin films, nanowires, and nanoparticles. The term "quantum dot" is frequently used to describe nanoparticles, which are essentially zero-dimensional entities [12]. The unique properties of the systems mentioned, which are applications of Basic Physics, are comprehensively explained through theoretical research. A fundamental aspect of understanding these systems involves the concept of the density of states (DOS) for different quantum structures: quantum dots (0 dimension), quantum wires (1 dimension), and quantum wells (2 dimensions). In solid-state and condensed matter physics, the density of states (DOS) refers to the number of available states per energy interval at each energy level that can be occupied. The DOS is inherently influenced by the dimensional constraints of the material in question. Hence, a concise explanation of the DOS is crucial for grasping the behavior and characteristics of these quantum systems [13].

The units used to display dimensions are DOS (Energy-1 Volume-1). A volume becomes an area at the limit when the system has two dimensions, and a length at the limit where the system only has one dimension. Remember that the volume being discussed is the volume of k space, which is the area bounded by the constant energy surface of the system, and that this volume is obtained using a dispersion relation between E and k. The electronic band structure of a material controls the dispersion relation for electrons within it [14].

The available electron states in a system can be calculated by the well-known Schrodinger's equation:

$H \Psi = E\Psi$

The general expression to obtain the density of states in k-space/volume is as follows:

$N(E)dE \propto$ E^(d/2 -1) dE d=1,2,3

In this situation, where d is the degree of dimension, the energy is computed from the top of the valence band for holes and the bottom of the conduction band for electrons. In the three-dimensional (3-D) system, N(E) is an energy function with a smooth square-root form. A 2-D system varies greatly from a 3-D system because N(E) in a 2-D system is constant. The energy spectrum is quasi-continuous even though the density of states in a 2-D system is a step function [15]. Every time we go to a system with smaller dimensions, the DOS's reliance on energy changes by an order of magnitude, or E-1/2.

1.4.1 Zero-dimensional materials (0-D)

Materials larger than 100 nm, where all dimensions are at the nanoscale, are classified as 0-D. The most common type of zero-dimensional nanomaterials are nanoparticles, which can be made from metallic, ceramic, or polymeric substances and come in various shapes and sizes. These nanoparticles can exist independently or as part of a matrix, and they may consist of one or more chemical elements. They can also be amorphous, crystalline, single-crystalline, or polycrystalline. In 0-D nanomaterials, electrons are confined in three-dimensional space, preventing them from migrating or becoming delocalized [17].

1.4.2 One-dimensional materials (1-D)

As a result, nanoparticles are formed with a needle-like shape in one dimension that is not minuscule. One-dimensional materials encompass nanotubes, nanorods, and nanowires. These 1-D nanomaterials can exist as standalone entities or be incorporated into other media. They can be metallic, ceramic, polymeric, single-crystalline, or polycrystalline, and may be chemically pure or impure [18], One-dimensional nanomaterials can be amorphous or crystalline, single-crystalline or polycrystalline, or any combination of these forms. In these materials, delocalization happens along the long axis of the nanowire, nanorod, or tube, whereas electron confinement is observed in two dimensions.

1.4.3 Two-dimensional materials (2-D)

Materials that lack dimensional constraints within the nanoscale range are commonly known as bulk nanomaterials. These materials are typically defined by their three dimensions, which are arbitrarily set to be greater than 100 nm. They may have a nanocrystalline structure or display properties at the nanoscale. Bulk nanomaterials are composed of nano-sized crystals

arranged in various orientations, frequently showing nanocrystalline formations [19]. Three-dimensional nanomaterials, characterized by their nanoscale attributes, encompass a variety of structures including multi-layered nanostructures, clusters of nanowires and nanotubes, and distributions of nanoparticles. In these 3-D nanomaterials, electrons are fully delocalized.

1.5 Optical and Electrical properties of nanomaterials

1.5.1 Transmittance and Absorption

The size of particles significantly influences the transmission and absorption properties of any substance. Materials at the nanoscale display unique characteristics that differ from their larger counterparts. External factors can be manipulated to alter these properties. As particle size decreases, there is a higher likelihood of carrier confinement at the quantum level, and this phenomenon becomes more pronounced with further size reduction [20]. The inclusion of dopants can influence and modify the band gaps. This variation in band gap is frequently linked to changes in lattice properties, which can occur through processes like annealing [21,22] or impurity doping [23,24].

1.5.2 Electrical conductivity

The charge transfer phenomena in nanoscale materials are primarily influenced by the presence of grain boundaries [25]. The interface of the grain boundary has a notable influence because of its elevated density of defects, such as vacancies, dangling bonds, and vacancy clusters [26]. As a result, the presence of an external field can facilitate charge transport across grain boundaries through mechanisms like dipole reorientation, electronic relaxation polarization, and space charge dispersion. Grain boundary defects play a significant role in modifying the dielectric properties of a material, especially when subjected to external heating conditions.

1.6 What are the reasons for studying and using 2-dimensional materials?

The field of nanomaterials, a branch of material science, centers on the investigation of substances that possess at least one dimension inside the nanoscale scale [27]. At this specific scale, the number of atoms or molecules that make up a substance leads to noticeable changes in its physicochemical properties and reactivity. This size-dependent behavior is evident in various phenomena, such as the quantum confinement observed in semiconductor particles, the surface plasmon resonance found in metal nanoparticles, and the superparamagnetism exhibited by magnetic nanomaterials.

When a material is constrained to only one dimension, it forms a layered or two-dimensional (2D) structure. If it is confined to two dimensions, the material takes on a wire-like or one-dimensional (1D) structure. When all three dimensions are restricted to just a few nanometers or less, the material is often referred to as zero-dimensional (0D).

Dimensionality, rather than just size, is a key factor in defining a material's properties. This is especially relevant for sp2 carbon materials, which display a variety of unique characteristics depending on their dimensional structure. For example, 0-dimensional (0D) fullerenes, 1-dimensional (1D) nanotubes, 2-dimensional (2D) graphene, and 3-dimensional (3D) graphite each exhibit distinct properties. Carbon provides a striking example of the evolution in understanding various dimensional forms of a substance. Since the sixteenth century, graphite has been extensively used in industrial applications, playing a vital role in steel production, brake linings, and as a dry lubricant. The discovery of fullerenes in 1985 significantly broadened the knowledge of carbon allotropes, leading to the identification of carbon nanotubes in 1991. This progression underscores the importance of exploring different dimensional configurations to fully understand a material's potential.

The use of individual graphite layers as initial substances for theoretical examinations of graphite, fullerenes, and nanotubes has been documented. However, the successful isolation of a single-layer graphene sheet was not achieved until 2004 [28]. The recent wave of academic research on graphene highlights the profound scientific interest in this material and its potential applications across various technological sectors. Two-dimensional materials, including graphene, are anticipated to significantly influence numerous fields. These fields include electronics, gas storage and separation, catalysis, high-performance sensors, support membranes, and inert coatings, among others. This surge in research underscores the excitement and promise that 2D materials hold for advancing technology and innovation in these areas.

A vast number of publications and studies have thoroughly explored the fabrication methods and physical properties of graphene. The findings from these investigations have spurred the development of other innovative two-dimensional materials. Despite this progress, the current literature on the subject is still limited and fragmented. This review seeks to highlight the existing literature on the concepts and techniques related to the isolation and characterization of graphene. It suggests applying these established methods to a new group of 2D materials,

aiming to provide a comprehensive understanding of the topic. Additionally, it presents new perspectives and potential applications for these two-dimensional materials.

When size constraints are applied to one or more dimensions, certain material properties are altered. Consequently, two-dimensional (2D) materials often display unique characteristics compared to their bulk counterparts. These distinct optical and electrical properties can be attributed to the confinement of electrons and the absence of interlayer interactions. Although interlayer interactions are typically modest, they significantly influence the band structure. The variations in properties, such as mechanical strength and chemical reactivity, are mainly driven by geometric factors and the substantial surface-to-volume ratio, which can become exceedingly large in extremely thin materials.

1.7 Dye Removal from Wastewater

The rapid industrialization and urbanization over the past few decades have led to a significant increase in the discharge of industrial effluents into water bodies, posing severe environmental and health hazards. Among these pollutants, synthetic dyes are particularly concerning due to their complex chemical structures, which make them resistant to degradation and removal by conventional wastewater treatment methods. Textile, paper, and dye manufacturing industries are the primary contributors to dye pollution, releasing substantial quantities of coloured wastewater into the environment [29].

Dyes in wastewater can cause several environmental issues, including reduced light penetration in water bodies, which affects photosynthetic activity and disrupts aquatic ecosystems. Moreover, many dyes and their degradation products are toxic, mutagenic, or carcinogenic, posing significant risks to human health and aquatic life [30]. Therefore, the development of efficient and sustainable dye removal technologies is crucial.

Molybdenum disulfide (MoS_2), a two-dimensional transition metal dichalcogenide, has emerged as a promising material for various environmental applications, including dye removal from wastewater. MoS_2 possesses unique structural, electronic, and catalytic properties, making it an excellent candidate for adsorptive and photocatalytic degradation of dyes. Its high surface area, tunable electronic properties, and ease of functionalization further enhance its applicability in wastewater treatment [31].

The adsorption process is one of the most effective methods for dye removal, owing to its simplicity, cost-effectiveness, and high efficiency. MoS_2-based adsorbents have shown exceptional performance in adsorbing a wide range of dyes from aqueous solutions. The layered structure of MoS_2 provides abundant active sites for dye adsorption, and its chemical stability ensures durability under various environmental conditions [32]. Additionally, the modification of MoS_2 with functional groups or the incorporation of other materials can enhance its adsorption capacity and selectivity for specific dyes.

Photocatalysis, another promising approach, involves the degradation of dyes under light irradiation. MoS_2 exhibits excellent photocatalytic properties due to its narrow bandgap, which allows it to absorb visible light and generate electron-hole pairs necessary for the degradation of organic pollutants. The incorporation of MoS_2 into composite materials or its combination with other photocatalysts can further improve its photocatalytic efficiency and stability [33].

Recent studies have demonstrated the potential of MoS_2 in removing various dyes, such as methylene blue, rhodamine B, and methyl orange, from wastewater. For instance, MoS_2 nanosheets exhibited a high adsorption capacity for methylene blue, with a maximum adsorption capacity of 302 mg/g [32]. Similarly, MoS_2-based photocatalysts have shown significant degradation efficiencies for different dyes under visible light irradiation [34].

The application of MoS_2 in dye removal from wastewater represents a promising solution to address the environmental challenges posed by dye pollution. Its unique properties, including high surface area, excellent adsorption capacity, and photocatalytic activity, make it a versatile material for efficient and sustainable wastewater treatment. Further research and development in this field can lead to the optimization of MoS_2-based systems and their large-scale implementation in industrial wastewater treatment processes.

1.8 What is MoS_2?

Molybdenum disulfide (MoS_2), a transition metal dichalcogenide (TMD), has garnered significant attention in recent years due to its unique properties and potential applications [31]. MoS_2 is a layered material composed of molybdenum and sulfur atoms arranged in a hexagonal lattice structure [35]. Its layered structure, similar to graphene, offers high surface area, chemical stability, and tunable electronic properties [36].

MoS_2 has been explored for various applications, including electronics, energy storage, catalysis, and biomedicine [37]. Its high carrier mobility and optical absorbance make it suitable for electronic devices and photovoltaic applications [38]. Additionally, MoS_2 has shown promise as a catalyst for hydrogen evolution reaction (HER) and as a material for lithium-ion batteries [39].

Recent advances in synthesis methods have enabled the production of high-quality MoS_2 nanosheets with controlled thickness and size [40]. Mechanical exfoliation, chemical vapor deposition, and sol-gel processing are some of the commonly used methods [41].

The unique properties of MoS_2 make it an attractive material for various industries. Its biocompatibility and biodegradability have opened up opportunities in biomedicine, including drug delivery and imaging agents [42]. Furthermore, MoS_2 has shown potential in environmental applications, such as wastewater treatment and gas sensing [43].

1.8.1 Structure and polymorphs

MoS_2 has three different polymorphs:

1. 1T- exhibits a trigonal Bravais lattice structure
2. 2H- exhibits a hexagonal Bravais lattice structure (considered to be the most stable configuration of MoS_2)
3. 3R- exhibits a rhombohedral Bravais lattice structure

Such polymorphic qualities lead to multiple MoS_2-based materials with widely varying characteristics by slightly changing the operating parameters during synthesis

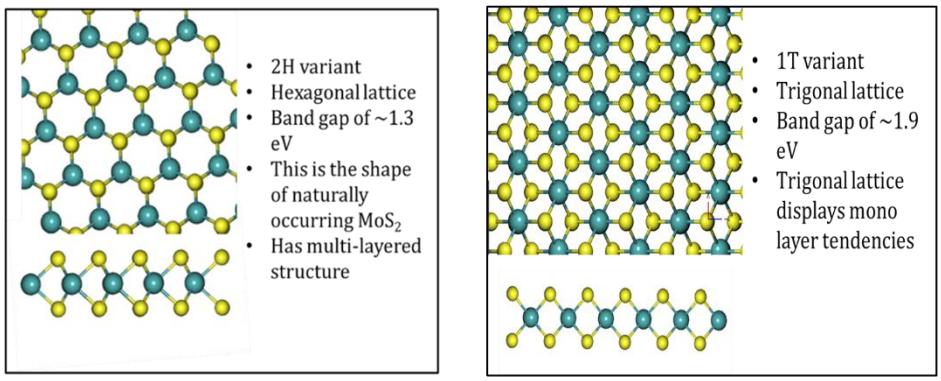


Figure 1: Different Structures of MoS_2

1.8.2 Application of MoS_2

MoS_2 nanomaterials are used in different application area like -

1. Hydrogen Evolution Reaction
2. Electrochemical Supercapacitors
3. Photocatalytic water splitting
4. Electrode Material of Sodium Ion Battery
5. Dye Sensitized Solar Cells
6. Photodegradation Of Organic Compounds in Wastewater
7. Electromagnetic Wave Absorption

1.8.3 Different synthesis methods of MoS_2:

The synthesis process included the use of both top-down methods, including mechanical exfoliation [44, 45] and chemical exfoliation [46– 48], as well as bottom-up approaches, such as chemical vapor deposition on substrates [49, 40] and chemical synthesis [50,42]. Various approaches have been used for the synthesis of MoS_2 as a co-catalyst.

I. Chemical Vapor Deposition (CVD):

This process involves the reaction of molybdenum-containing compounds (such as MoO_3) with sulfur vapor at high temperatures. It produces high-quality and large-area MoS_2 films with good control over thickness and morphology. However CVD requires high temperatures and sophisticated equipment, making it expensive and complex.

II. Exfoliation:

The exfoliation process involves the mechanical or chemical exfoliation of bulk MoS_2 crystals into monolayers or few-layered nanosheets. This process is simple and effective for producing high-quality monolayers. But it produces very low yield and faces scalability issues and mechanical exfoliation is time-consuming.

III. Liquid-Phase Exfoliation:

In Liquid-Phase Exfoliation bulk MoS_2 is dispersed in a solvent and sonicated to produce nanosheets. This process is good for producing large quantities of nanosheets. The resulting nanosheets often have a wide size distribution and may contain defects.

IV. Hydrothermal Synthesis:

Hydrothermal synthesis involves the reaction of molybdenum and sulfur precursors in a sealed vessel under high temperature and pressure in an aqueous or non-aqueous medium. This process is simple, cost-effective, and can produce MoS_2 with various morphologies (e.g., nanoparticles, nanoflowers, nanosheets). The process has better control over the crystal structure and size. It requires careful control of reaction conditions like temperature, pressure, and concentration to achieve desired properties.

Table 2: Methods of synthesis of MoS_2

Precursors		**Additional Chemicals**	**Parameters in hydrothermal route**		**Structure of MoS_2 obtained**	**Application Analysed**	**Reference**
Molybdenum	**Sulphur**		**Temperature**	**Time**			
Ammonium Heptamolybdate Tetrahydrate	Thiourea	NA	220ºC	1 Hour	Nano-flakes	Enhanced Energy Storage capability	(S. Rani et al., 2023)
			220ºC	3 Hour	Nano-flowers		
			180ºC	24 Hour			
			220ºC	12 Hour	Micro-flowers		
				24 Hour			
				50 Hour			
Ammonium Molybdate Tetrahydrate	Thioacetamide	NA	180ºC	18 Hour	Flake shaped	Electromagnetic Wave Absorption	(Feng et al., 2020)
		Hexadecyl Trimethyl Ammonium Bromide	180ºC	18 Hour	Flower shaped		
Ammonium Heptamolybdate Tetrahydrate	Thiourea	NA	200ºC	22 Hour	Flower shaped	Thermal Battery	(Zheng et al., 2018)
Sodium Molybdate	Thioacetamide	NA	220ºC	24 Hour	Nano-flakes	Multiple Wavelength Optical	(Chaudhary et al., 2018)

						Sensing Applications	
Sodium Molybdate	Thioacetamide	Carbon Fiber Cloth	180°C	8 Hour	Trigonal Lattice	Hydrogen Evolution	(Liu et al., 2019)
			220°C	24 Hour	Honeycomb-Like Lattice		
Ammonium Molybdate Tetrahydrate	L-Cysteine	NA	180°C	30 Minute	Flower shaped	Hydrogen Evolution Reaction	(Solomon et al., 2020)
			180°C	24 Hour			
Ammonium Molybdate Tetrahydrate	Thioacetamide	NA	180°C	6 Hour	3D Flower Shaped	Photocatalytic Hydrogen Energy Production	(Nadeem Riaz et al., 2019)
			200°C	12 Hour			
			220°C	24 Hour			
		La^{3+}	200°C	24 Hour			
Ammonium Molybdate Tetrahydrate	Thiourea	NA	120°C	15 Hour		Visible Light Photocatalytic Degradation Of Organic Dyes	(A. Rani et al., n.d.)
			140°C				
			160°C				

2 LITERATURE REVIEW

2.1 Literature review on the synthesis of MoS_2 nanomaterial

Several methods of synthesis of MoS_2 nanomaterial have been investigated, as seen from Table 2. Hydrogen fuel is expected to replace traditional fuels that produce hazardous effects on our environment [116]. Hydrogen production from water splitting reactions is a viable technique for clean sustainable energy production [117]. Due to larger band gap and higher electron-hole pair recombination, photocatalysts like TiO_2, and ZnO_2 have lower light absorption ability [118-121]. MoS_2 has gained significant consideration in the material science field due to its outstanding electronic properties, chemical properties, efficient catalytic properties, appropriate band gap energy, and diverse applications [122-124]. MoS_2 is a two-dimensional material having a sandwiched structure obtained from molybdenum (Mo) atoms and hexagonal close-packed sulfur (S) (S-Mo-S) [125,126]. The van der Waals forces combine the layered structure of MoS_2, which can be exfoliated into one or few-layered nanosheets [127]. Despite its excellent properties as a photocatalyst, MoS_2 suffers from the shortcoming of the high rate of charge carrier's recombination and development of Mo-S-O links during the photocatalytic process [128]. MoS_2 nanostructures had better adsorption ability and photocatalytic performance for hydrogen production but, are difficult to manufacture. Lanthanum (La) is a rare earth element that can reduce recombination in photocatalysis. The influence of La on morphology and photocatalytic properties of MoS_2 was studied. Three-dimensional (3D) flower-like MoS_2 nanostructures were prepared via facile and cost-effective hydrothermal method by varying hydrothermal temperatures (180°C, 200°C, and 220°C) and reaction time (6, 12, 24, and 36 hours). The sample prepared at 200°C for 24 hours has a 3D flower-like MoS_2 nanostructure. Upon modification with La improved specific surface area and optical properties. The photocatalytic performance of La-doped MoS_2 was observed to be 5.2 times higher than pure MoS_2 [129]. Hydrothermal synthesis of Molybdenum disulfide (MoS_2) with varying morphologies and its efficacy in adsorbing bisphenol A (BPA), a common endocrine disruptor is studied. The research investigates the influence of preparation conditions such as the molar ratio of sulfur to molybdenum (S/Mo), hydrothermal temperature, and time on the morphologies of MoS_2. Various characterizations including X-ray diffraction (XRD), field emission scanning electron microscopy (FESEM), transmission electron microscopy (TEM), X-ray photoelectron spectroscopy (XPS), Raman spectra, and Brunauer-Emmett-Teller (BET) surface area measurement were utilized to examine the synthesized materials. Three distinct morphologies of MoS_2-coral like aggregated particles, flower-like spheres, and wrapped nano-

sheets were achieved by manipulating the hydrothermal conditions. Increasing hydrothermal temperature and time progressively transformed the MoS_2 morphology. This morphological control is significant for specific applications in different fields. The synthesized MoS_2 materials demonstrated high adsorption capacity (39.03 mg/g) and fast adsorption rates (0.0053 g/(mg/min)) for BPA, making them effective adsorbents [130]. The adsorption process was found to be thermodynamically exothermic and spontaneous, with strong electrostatic and π-π interactions between BPA and the MoS_2 materials being crucial for BPA adsorption. The study concludes that MoS_2 synthesized with a 3:1 S/Mo ratio, at 240°C for 37 hours, exhibited the best adsorption properties due to its high specific surface area and large pore volume. These findings highlight the potential of MoS_2 materials for environmental applications, particularly in removing harmful endocrine disruptors like BPA from water. The study compares microwave-assisted and conventional hydrothermal synthesis of MoS_2 nanosheets and evaluates their effectiveness as catalysts for the hydrogen evolution reaction (HER) [131]. MoS_2 nanosheets were synthesized using both methods, with microwave synthesis completed in 30 minutes and hydrothermal synthesis taking 24 hours. The microwave method produced nanosheets with a less crumpled structure and smoother edges compared to the hydrothermal method. Characterization techniques, including XRD, Raman spectroscopy, and TEM, confirmed that both synthesis methods resulted in MoS_2 with similar crystal structures, but with differences in morphology. The hydrothermal method yielded very short-range ordered wrinkle nanosheets, whereas the microwave method produced smoother, interconnected nanosheets. Electrochemical testing showed that HT-MoS_2 required an overpotential of -280 mV to achieve a current density of 10 mA/cm², while MW-MoS_2 required -320 mV, indicating that HT-MoS_2 was more active in the faradic region. Additionally, HT-MoS_2 exhibited a lower Tafel slope (165 mV/dec) compared to MW-MoS_2 (201 mV/dec), suggesting improved HER kinetics. The electrochemical impedance spectroscopy (EIS) measurements further supported these findings, showing lower charge transfer resistance for HT-MoS_2 (354.4 ohms) compared to MW-MoS_2 (401 ohms). In summary, while both synthesis methods produced MoS_2 nanosheets with similar structural properties, the hydrothermal method resulted in better electrocatalytic performance for HER due to the more active sites created by the short-range ordered wrinkle nanosheets. However, the microwave method's advantages include shorter synthesis time and energy efficiency. MoS_2 can be an important electrocatalyst for hydrogen evolution reactions owing to its catalytically active edge sides [102-105]. Increasing the number of exposed active sites can enhance the electrocatalytic activity of MoS_2 [106]. 2-D MoS_2 nanosheets stack together easily through van der Waals force along the (002) plane,

which severely decreases the number of active sites because the (002) plane is the inert plane for HER [107, 108]. However, because the (002) plane was the thermodynamically stable plane among all the lattice planes of MoS_2 which was very easy to form, it was a challenge to control the growth of the (002) plane to get MoS_2 with more active sites for HER. Thus, efforts like mechanical exfoliation, chemical exfoliation, and chemical synthesis have been made to disrupt stacking the (002) plane and get single-layer MoS_2 with more exposed active sites [108-114]. A facile hydrothermal method to synthesize MoS_2 nanosheets with different (002) intensities under acidic, alkaline, and neutral conditions is studied to investigate the effect of pH on the structure of MoS_2. MoS_2 is synthesized at 240 ◦C for 24 h. XRD was used to analyse the three different samples. Acidic MoS_2 shows the smallest size and stacking layers which means more active sites. The electrocatalytic measurements for HER show acidic MoS_2 exhibit not only the highest activity for HER but also the largest capacitance [115]. Therefore, low pH is helpful for decreasing the stacking of MoS_2 sheets along the (002) plane.

2.2 Literature review on applications of MoS_2 nanomaterial

In the bid to produce sustainable clean energy, hydrogen can be considered a good source. The conventional method of generating that produces CO_2 as a byproduct. Hence, we consider the generation of hydrogen from a water-splitting reaction using 2D NMs. 2D NM TMDS, specifically MoS_2 can be used effectively for the HER and OER reactions due to its layered structure, high surface area, strong in-plane covalent bonding, and small distance traveled by charge carriers. MoS_2 may be manufactured via the hydrothermal method as seen in Table 2, which would benefit from lowered reaction temperature and homogeneity of nanomaterial [51].

2.2.1 Hydrogen Evolution

MoS_2 synthesized in its thermo-stable polymorph of 2H-phase has limited edges, large inert basal planes, and being a semiconductor, it is not conducive to the electrolytic process [52-56]. 1T- MoS_2 does not have the above negative effects and can be used as HER electrocatalyst [57-59]. A vertically layered self-supported structure can be beneficial in providing abundant active sites to catalyze HER. To prepare the 1T- MoS_2, 0.1mmol ammonium molybdate, and 0.5mmol thiourea were dissolved in a mixture of 2:1 ratio of water and propionic acid by volume. The

homogeneous solution was transferred to an autoclave and a piece of carbon fiber cloth was inserted. The autoclave was heated at 180℃ for 8 hours. The MoS_2 nanosheets are vertically oriented and uniformly distributed over the entire surface of carbon fibers, leaving substantial voids among them [60]. Two distinct kinds of lattice are formed- a trigonal lattice that manifests in the presence of 1T phase, at 180℃ for 8 hours, and a honeycomb-like lattice for the 2H phase at 220℃ for 24 hours, confirming the existence of two kinds of polymorphs. The as-prepared 1T- MoS_2 was used as an electrode for HER and was found to have superior performance over 2H-MoS_2 and powdery 1T-MoS_2. The outstanding catalytic activity of 1T-MoS_2 arises from the following aspects:

a) 1T-phase MoS_2 with an active basal plane and metal-like conducting feature provides abundant active sites and high conductivity;

b) the self-supported structure free from the "binder-block-effect" ensures efficient access to active sites, and the highly conductive carbon fiber framework facilitates electron transfer throughout the electrode. The synergistic effect of 1 T-phase of MoS_2 and the self-supported structure enables 1 T-MoS_2 as a highly active HER electrocatalyst [60]. Self-supported architecture of 1T- MoS_2 is found to have excellent thermal and chemical stability as well.

2.2.2 Enhanced Energy Storage Capability

Sustainable energy needs to be stored sustainably in supercapacitors (SCs). TMDs, especially MoS_2 are suitable SC materials due to their large surface area, layered morphology, chemical stability, and tunable conductivity [61-63]. Most recent studies have focused on MoS_2 hybrids in order to boost capacitive performance [62-70]. Understanding the relation between various growth parameters (reaction time, temperature, amounts of precursors) influencing the structural properties and the electrochemical performance of bare MoS_2 nanostructures can be further utilized in hybrid/composite architecture [71]. MoS_2 nanoflowers have been synthesized via a one-step hydrothermal route. The role of growth parameters that affect the crystallinity, inter-layer spacing, and intra-layer defects on the electrochemical properties has been studied for the bare MoS_2 nanostructures [71]. A facile one-step hydrothermal route utilizing ammonium heptamolybdate tetrahydrate and thiourea was used and the colorless

solution was transferred to an autoclave after stirring. Crystallinity and phase of MoS_2 samples synthesized at different temperatures (150, 180, 220 & 260 ℃) for the reaction time of 24 h were analyzed with the aid of XRD. The samples synthesized at the 150 ℃ have shown the cluster-like morphology which can be attributed to growth of MoO_3, which was previously confirmed by XRD. The samples synthesized at 180 ℃ for 24 hours represents the mixture of MoO_3 grains and MoS_2 flakes and have a nano-flower structure. The nano-flower-like morphology was obtained at 220 ℃ while merging of these flowers to form larger micro-flowers of MoS_2 at 260 ℃ can be noticed [71]. The results in this study indicate an effective way of tuning the inter-layer spacing with reaction time, and its correlation with the electrochemical performance of MoS_2.

2.2.3 Electromagnetic Wave Absorption Property

With the wide use of electromagnetic waves in the modern world, there is a need for EMW-absorbing materials to reduce pollution. Due to its physical and chemical properties, MoS_2 can be considered an EMW absorber. The effect of morphology on EMW absorption is studied. Flower-shaped MoS_2 was obtained by mixing a solution of ammonium molybdate tetrahydrate and thioacetamide dissolved in deionized water and a solution of hexadecyl trimethyl ammonium bromide dissolved in water. The mixture was transferred to an autoclave and maintained at 180℃ for 18hr. Ethanol absolute was added to a solution of ammonium molybdate tetrahydrate and thioacetamide dissolved in deionized water, transferred to an autoclave, and maintained at 180℃ for 18 hr to obtain flake-shaped MoS_2 [72]. The morphology and microstructure were studied by SEM and TEM. It is found that flower-shaped MoS_2 nanoparticles have a much broader effective EMW absorption bandwidth than that of flake-shaped MoS_2 nanoparticles, and the thickness of the minimum RL value is less than that of flake-shaped MoS_2 nanoparticles. The difference in the EMW absorption properties of the two samples could be attributed to the polarization effect of the sample under the electromagnetic field and the different morphology of the two samples. The EMW will undergo multiple reflections in the flower-shaped MoS_2 nanoparticles because of the special structure which leads to a broad effective bandwidth [72]. Hence, it can be concluded that flower-shaped MoS_2 has better EMW absorption owing to its larger specific surface area.

2.2.4 Multiple Wavelength Optical Sensing Applications

2D MoS_2 is an optically active and interesting material for device applications such as chemical sensors, electronic devices, photodetectors, etc. [73-77]. MoS_2 based optical sensors can be used in the visible light spectrum [78]. Hydrothermally produced sheet-like morphology of MoS_2 at optimized temperature 180℃ and 24 hours is studied. X-Ray Diffraction (XRD), Scanning Electron Microscopy (SEM), Transmission Electron Microscopy (TEM), Raman, and UV–vis spectroscopy were carried out to characterize the synthesized MoS_2 nanosheets. SEM and TEM images showed the morphology of ultrathin nanosheets of MoS_2. The optical sensor of MoS_2 nanosheets was fabricated and thoroughly studied using various laser excitation wavelengths (λe_x): 440 nm (indigo); 460 nm (blue); 550 nm (green); 570 nm (yellow); 635 nm (red) and 785 nm (infra-red). Current reduced quickly when laser illumination was turned off, and recovered to its original state. Optical sensing is stable and reproducible over several lights on and off cycles. The fabricated optical sensor showed maximum sensitivity to the red laser source and exhibited the best response in the visible range of spectrum. The photo response is found to be linearly dependent on optical power density [78].

2.2.5 Thermal Battery

Thermal battery is a class of primary battery in which the electrolyte is in solid state at room temperature, and melts into molten salt when the battery is activated. Pyrite is typically used as a cathode but isn't beneficial due to its poor thermal stability and high impedance during discharge. The layered structure of MoS_2 stacked by weak Van der Waals force allows easy intercalation of foreign ions [79]. Therefore, MoS_2 is expected to replace pyrite in the field of thermal batteries [80-93]. The morphology, thermal stability, and electrochemical performance of different kinds of MoS_2 microspheres are observed and compared. A mixture of ammonium heptamolybdate tetrahydrate and thiourea dissolved in deionized water was transferred to a Teflon-lined stainless-steel autoclave and heated at 220℃ for 22 hr, to produce flower-shaped MoS_2. The flower-like porous MoS_2 microsphere with good crystallinity consisted of MoS_2 nano-sheets with a thickness of about 10 nm. The evolution process of the flower-like MoS_2 crystals was proposed, which begins with a nucleus growth process, followed by MoS_2 nano-sheet growth and self-assembly [94]. MoS_2 is found to be stable until 700℃ and has the best thermal stability as compared to CoS_2 and FeS_2 which begin to lose weight at 500℃ or 650℃. The melting heat of electrolyte reduces when MoS_2 is used as cathode material in the thermal battery. The electrochemical analysis showed that the thermal battery had the longest discharge

time and largest capacity when using the MoS_2 samples with flower-like porous microsphere structure as cathode, compared with MoS_2 samples with other structures, FeS_2 or CoS_2 [94].

2.2.6 Visible Light Photocatalytic Degradation of Dyes

Photocatalysis is an effective way to degrade pollutants [95,96]. TMDs, particularly MoS_2 can be used for photocatalysis due to its tunable band gap that compresses the electron-hole recombination rates, making MoS_2 self-excited under visible and UV light irradiation [97-100]. The structure of the catalyst affects the charge transfer process responsible for the catalytic activity and the effects of MoS_2 synthesized by two routes have been compared. In the MoS_2 prepared by hydrothermal route, ammonium molybdate tetrahydrate and thiourea solution in deionized water was transferred to an autoclave and the reaction was carried out at 120, 140, and 160℃ for 15 hr. MoS_2 has also been prepared by liquid-exfoliation method using sonification. Degradation of organic dyes MR and MB by MoS_2 NSs synthesized by both routes have been studied by illumination under UV–Vis light. The as-synthesized photocatalysts characterized by XRD reveal that the exfoliated NSs from the sonication method at room temperature exhibit sharp and intense diffraction peaks inferring better crystallinity than NSs prepared at 160℃ - 15 h by conventional hydrothermal method. For both the synthesis routes, the difference of *25 cm-1 appears between the E1 2g and A1g modes of Raman spectra, indicating the presence of 5–6 layers of MoS_2. Among these three routes, hydrothermally synthesized MoS_2 NSs exhibit the least degradation efficiency with 58.92% for MR and 49.28% for MB. Simultaneously, the exfoliated MoS_2 NSs in NMP act as a better photocatalyst for the degradation with 63.40% for MR and 62.40% for MB. The lower efficiency of the MoS_2 NSs prepared by the hydrothermal method might be due to the re-aggregation of sheets and the availability of a lesser number of active sites essentially needed for the photocatalytic activity [101].

Table 3: Synthesis of MoS_2 nano-composites

Synthesized Nano Composite	**MoS_2 Precursors**		**Other Constituents**	**Preparation method of constituents**	**Method of incorporation**	**Application**	**References**
	Mo	**S**					
Fe_3O_4@MoS_2/RGO	Sodium Molybdate	Thioacetamide	RGO	Hummers Method	Simultaneous Hydrothermal treatment	Electrochemical Hydrogen Evolution and Methanol Oxidation	(Askari et al., 2019)
			Iron(III) Oxide	Rapid hydrothermal method			
MoS_2-NiS/CdS	Sodium Molybdate	Thiourea	Cadmium sulfide	Hydrothermal treatment of $CdCl_2$	Gradual addition during Hydrothermal Treatment	Enhanced Photocatalytic Hydrogen Production	(Yin et al., 2019)
			NiS	Hydrothermal treatment of $NiSO_4$			
MoS_2@ZnO	Sodium Molybdate	Thiourea	zinc acetate	Sol-gel	Simple Hydrothermal Treatment	Photoluminescent Enhancement	(Khan et al., 2020)
			Cetyltrimethylammonium bromide				
Ni/MoS_2	ammonium heptamolybdate	Thiourea	nickel nitrate hexahydrate	NA	Hydrothermal Treatment followed by an annealing proces	Electrochemical Hydrogen Production	(Kumar et al., 2023)
MoS_2/TiO_2	Sodium Molybdate Dihydrate	Thiourea	TiO_2		Hydrothermal Followed By Quenching Method	Photocatalytic Hydrogen Production	(F. J. Zhang et al., 2019)
MoS_2/CeO_2	Sodium Molybdate Dihydrate	Thioacetamide	Cerium(IV) oxide	Rapid hydrothermal method	two-step hydrothermal reaction	ethanol gas sensing	(J. Zhang et al., 2021)
Ti_3C_2-MoS_2	Sodium Molybdate Dihydrate	Thiourea	Ti_3C_2	Etching of Al atom layers using HF	Simple Hydrothermal Treatment	Removal Of Pesticides	(Guo et al., 2022)
AgNPs/MoS_2/$NaTaO_3$	Sodium Molybdate	Thioacetamide	AgNPs	Photochemical Reduction	Facile Hydrother	Enhanced Photocatalytic Activity	(Y. Zhang et al., 2023)

			$NaTaO_3$	Two Step Hydrothermal Treatment of Ta_2O_5	mal Treatment		
$BiFeWO_6/MoS_2$	Sodium Molybdate	Thioacetamide	$BiFeWO_6$	Co-Precipitation Followed By Solvothermal Reaction	Facile Hydrothermal Process	Degradation Of Organic Pollutants	(Senthil et al., 2019)
MoS_2 QDs	Sodium Molybdate	L-Ascorbic Acid	NA	NA	Novel Hydrothermal-Solvothermal Cutting Integrated Route	photoluminescence	(Ren et al., 2018)
rGO/MoS_2	Ammonium tetrathiomolybdate		rGO	Hummers Method	Electronic Transport	humidity sensors	(Park et al., 2018)

$CoS_2@MoS_2$	Sodium Molybdate	Thiocarbamide	cobalt (II) nitrate hexahydrate	NA	Facile Solvothermal Method	High-Performance Supercapacitors	(Huang et al., 2018)
MoS_2@montmorillonite	Sodium Molybdate	Thioacetamide	Chitosan methyl orange sodium borohydride	NA	Facile Hydrothermal Treatment	photocatalytic activity and cycle stability	(Chen et al., 2020)
3D LSG_MoS_2_Ag NPs	Ammonium Heptamolybdate Tetrahydrate	Thiourea	Lignin-Based Laser-Scribed Graphene	Laser Scribing Method	Simple Hydrothermal Treatment	Troponin I Aptasensing	(Vasudevan, Remesh, et al., 2023)
			Ag NPs	NA			
MoS_2/RGO	Ammonium Heptamolybdate	Thiourea	RGO	Modified Hummers' Method	Facile Hydrothermal Treatment	Sonocatalytic Degradation Of Methylene Blue	(Zou et al., 2019)
$NiCo_2O_4/MoS_2$	Ammonium Heptamolybdate Tetrahydrate	Thiourea	$NiCo_2O_4$	Simple Solvothermal Method	Simple Solvothermal Method	Utilization Of Visible Light	(Li, n.d.)
MoS_2/C	Sodium Molybdate	Thiourea	Glucose	NA	Simple Hydrothermal Treatment	Electrochemical uses	(Song et al., 2018)

MoS2−Ag	Ammonium Heptamolybdate Tetrahydrate	Thiourea	Ag^+	Chemical Reduction of AgNO3	Facile Hydrothermal Treatment	Ultralow Detection Limit	(Kaushik et al., 2023)
LSG/MoS_2	Sodium Molybdate	Thiourea	Lignin-Based Laser-Scribed Graphene	Laser Scribing Method	Simple Hydrothermal Treatment	supercapacitor	(Vasudevan, Kanesan, et al., 2023)
MoS_2/SnS_2	Ammonium molybdate tetrahydrate	Thiourea	CH_4N_2S / $SnCl_4{\cdot}5H_2O$	Simple Hydrothermal Treatment	Facile Hydrothermal Treatment	Photocatalytic Activity	(Ma et al., 2023)

2.3 Literature review on the synthesis of MoS_2 nanocomposites

As seen in Table 3, numerous works have been carried out for the formation of MoS_2 nanocomposites.

2.3.1 Room temperature humidity sensors based on rGO/MoS_2 hybrid composites synthesized by hydrothermal method

New opportunities for gas sensors have opened up due to significant growth in the Internet of Things (IoT). Regulating and monitoring humidity has become very important in IoT, especially in automation, agriculture, aerospace, semiconductor industry and healthcare. Electronic type humidity sensors consist of capacitive and resistive types. Although the capacitive types offer numerous advantages and are extensively exploited, the complex and highly expensive fabrication process poses significant challenges. On the other hand, resistive type sensors are advantageous owing to features such as simple fabrication, cost-effectiveness, and small size which can be easily applied to sensor arrays. Metal oxides and polymers have not been found to be suitable candidates for fabricating resistive-type humidity sensors as it has been found that metal oxide-based humidity sensors show significant degradation of the sensor performance under humid ambient, while polymer-based humidity sensors exhibit inherent drawbacks of poor stability in high humidity environment, thus limiting their further development. Two-dimensional (2D) materials like graphene and transition metal dichalcogenides (TMD), with large surface-to-volume ratios, high specific area, and numerous active sites have demonstrated great potential as sensing materials. Reduced graphene oxide (rGO) is an excellent material for humidity detection as rGO has oxygen-containing functional groups such as COOH and OH on the surface which show hydrophilicity. Moreover, the fabrication of rGO is simple and cheap. MoS_2 is also an excellent humidity-sensing material

due to its remarkable sensing performance originating from dangling bonds at the edge sites. Considering the advantages of both materials, rGO/MoS_2 hybrid composites were utilized for humidity sensors. It has been found that when p-type rGO and intrinsic n-type MoS_2 come into contact, the p-n junction is formed by Van der Waals bonding between rGO and MoS_2. The p-n heterojunction formed between the rGO and MoS_2 interface enhances the humidity sensing performance of rGO and MoS_2 hybrid composites through controlling electronic transport at the hetero-interface and synergistic promotion of humidity sensing reaction. [132,133] 2D rGO/2D MoS_2 hybrid composites (MS-GOs) were synthesized hydrothermally. rGO and MoS_2 are mixed with different molar ratios and drop-casted on SiO_2 substrate with Pt interdigitated electrode. At an optimized molar ratio of rGO/MoS_2, the sensor device exhibits high sensitivity, good selectivity, rapid response and recovery, and good linearity for humidity sensing.[134] The enhanced sensing properties are attributed to the p-n junction between rGO and MoS_2.

2.3.2 One-step hydrothermal synthesis of a CoS_2@MoS_2 nanocomposite for high-performance supercapacitors

Supercapacitors possess excellent properties like rapid rechargeability, high power density, long cycle life, eco-friendly nature, and low-cost preparation. Although graphene exhibits fascinating properties and finds diverse applications in nanoelectronic devices, major restraints on its widespread use include high cost, low yield, and poor scalability. Hence the search for other suitable materials becomes important. MoS_2, a transition metal sulfide with a layered structure has ultrathin thickness and 2D morphology which leads to ultrahigh specific surface areas. Mo atoms can easily prompt redox faradaic reactions in the interlayer space due to oxidation states spanning a range from +2 to +6, and its theoretical specific capacitance could be as high as 1000 F/g [135,136]. These features make MoS_2 a promising electrode material to be used in supercapacitors. However, preparing a high-performance supercapacitor using MoS_2 as the electrode material still remains challenging due to low electrical conductivity and insufficient number of accessible active sites in MoS_2. Hence MoS_2 should be combined with a conductive material with high electrical conductivity to enhance the electrical conductivity and increase the content of accessible active sites. CoS_2 has the best conductivity, thermal stability, and superior capacitive behavior as its negative Gibbs free energy causes a spontaneous thermodynamic reduction reaction that is useful for pseudo-capacitance supercapacitors. So, a novel CoS_2@MoS_2 nanocomposite was synthesized by a facile one-step hydrothermal method. Initially, 2.5 mmol $Na_2MoO_4.2H_2O$, 1.25 mmol $Co(NO_3)_2.6H_2O$ (at a

Mo:Co molar ratio of 2:1) and 6.25 mmol H_2NCSNH_2 were dissolved in a 30 ml mixed solution of DI water and anhydrous ethanol (1:1 in volume). The precursor solution was magnetically stirred by ultrasonication for 30 min. The mixture was then transferred into a Teflon-lined autoclave, sealed, and heated in an oven at 180 ^oC for 48 h. After natural cooling to room temperature, the resulting black solid product was collected, then washed with DI water three times and ethanol three times before drying in a vacuum at 70 ^oC (referred to as CM-2). The number "2" refers to the molar ratio of $Na_2MoO_4.2H_2O$ and $Co(NO_3)_2.6H_2O$. CM-1 and CM-3 were synthesized by the addition of the corresponding quantity of $Co(NO_3)_2.6H_2O$ into the mixture with the same amount of $Na_2MoO_4.2H_2O$ (2.5 mmol). As reference materials, pristine MoS_2 and CoS_2 were also prepared, following the same procedure in the absence of $Co(NO_3)_2.6H_2O$ and $Na_2MoO_4.2H_2O$, respectively.[3] Following this, required characterization was carried out using X-ray diffraction, field-emission SEM, high-resolution TEM, and other important methods. It was found that the $CoS_2@MoS_2$ nanocomposite electrode shows a high specific performance of 1038 F/g at 1 A/g in a 2 M KOH solution. In addition, the $CoS_2@MoS_2$ nanocomposite electrode showed excellent cyclic stability and a high-rate capability contrasted with pure MoS_2 and pure CoS_2. The capacitance remained approximately 84.76% after 10000 cycles of charge-discharge at a current density of 5 A/g. The synergistic effect between MoS_2 and CoS_2 in the composite is expected to improve electrode performance when used as an electrode material for supercapacitors.[137] These excellent results indicate that the $CoS_2@MoS_2$ nanocomposite is a promising and suitable electrode material for high-performance supercapacitors.

2.3.3 Synthesis of unique-morphological hollow microspheres of MoS_2@montmorillonite nanosheets for the enhancement of photocatalytic activity and cycle stability

The research focuses on developing a novel photocatalyst to address environmental remediation challenges, specifically through the synthesis of MoS_2@montmorillonite nanosheets hollow microspheres (MoS_2@MMTNS-HMS). This material is designed with a unique hollow structure, featuring vertically aligned MoS_2 nanosheets on the surface of montmorillonite nanosheets (MMTNS). The aim is to enhance both photocatalytic activity and cycle stability. Molybdenum disulfide (MoS_2) is highlighted for its promising photocatalytic properties, primarily due to its visible-light absorption and intrinsic band gap. However, during synthesis, MoS_2 nanosheets tend to aggregate and stack, which significantly reduces their

photocatalytic efficiency [138]. To overcome these limitations, the research integrates MoS_2 with MMTNS, a layered clay mineral known for its large surface area, high cation exchange capacity, and swelling ability. The synthesis process employs an electrostatic layer-by-layer (LbL) assembly technique, where positively charged chitosan and negatively charged MMTNS are alternately deposited on polystyrene (PS) spheres. Following this, calcination is used to remove the PS core, and MoS_2 is then hydrothermally loaded onto the MMTNS-HMS to form the composite material [139]. Characterization of the synthesized MoS_2@MMTNS-HMS is conducted using various techniques, including scanning electron microscopy (SEM), transmission electron microscopy (TEM), X-ray diffraction (XRD), and X-ray photoelectron spectroscopy (XPS). These analyses confirm the successful synthesis and proper loading of MoS_2 onto the MMTNS-HMS. The unique morphology and structure are shown to enhance light-utilization efficiency and increase the density of edge active sites, which are essential for improving photocatalytic activity. The hollow structure allows better light penetration and interaction with the MoS_2 nanosheets, significantly increasing the effective surface area and active sites available for photocatalysis. The photocatalytic performance of the MoS_2@MMTNS-HMS is evaluated through the degradation of methyl orange (MO) under visible light irradiation. The results demonstrate that MoS_2@MMTNS-HMS exhibits significantly higher photocatalytic activity compared to pristine MoS_2 [139]. This enhancement is attributed to the hollow structure and optimal alignment of MoS_2 nanosheets, which facilitate better light absorption and utilization. The material's design maximizes light interaction and reduces the recombination of photogenerated electron-hole pairs, leading to improved efficiency. The study also explores the cycle stability of the composite material. The findings indicate that MoS_2@MMTNS-HMS maintains high photocatalytic performance over multiple cycles, with only a minor decrease in efficiency. This stability is primarily due to the inhibition of MoS_2 oxidation by the MMTNS-HMS support, preventing the degradation of the photocatalyst. The ability to retain performance across cycles underscores the material's potential for practical applications in environmental remediation, where long-term stability and efficiency are crucial.

2.3.4 Facile synthesis of MoS_2 nanoflower-Ag NPs grown on lignin-derived graphene for Troponin I aptasensing

The study details the development of a biosensor for detecting Troponin I, a biomarker for Acute Myocardial Infarction (AMI), using a hybrid material made from MoS_2 nanoflowers and

silver nanoparticles (Ag NPs) grown on lignin-derived graphene. This novel biosensor addresses the limitations of conventional methods for AMI detection, which are often time-consuming, expensive, and not environmentally friendly. The synthesis of the biosensor involves several key steps. Initially, lignin extracted from oil palm's empty fruit bunches is purified into lignosulfonate and converted into graphene through a laser scribing method. This method involves coating a glass substrate with a lignin solution, drying it, and then using a CO_2 laser to produce graphene. Next, biogenic silver nanoparticles (Ag NPs) are synthesized by adding a silver nitrate solution to a lignin solution, reducing the silver ions to Ag NPs with the aid of lignin. Subsequently, the 3D lignin-derived graphene (3D LSG) is combined with MoS_2 and Ag NPs through a hydrothermal method, resulting in the hybrid material 3D LSG_MoS_2_Ag NPs. This hybrid material is then used to modify screen-printed carbon electrodes (SPCE), which are chemically treated to immobilize a biotinylated aptamer that specifically binds to Troponin I [140] The hybrid material's unique properties are thoroughly characterized using various techniques. Field-emission scanning electron microscopy (FESEM) and transmission electron microscopy (TEM) reveal the morphology of the 3D LSG_MoS_2_Ag NPs, showing petal-like MoS_2 nanoflowers with Ag NPs embedded on the graphene surface. X-ray diffraction (XRD) confirms the crystallinity and plane orientation of the materials, while Fourier-transform infrared spectroscopy (FT-IR) identifies the functional groups present in the hybrid. X-ray photoelectron spectroscopy (XPS) further validates the successful synthesis and interaction of the components within the hybrid material [140]. The biosensor's performance is evaluated using Electrochemical Impedance Spectroscopy (EIS). The EIS measurements demonstrate the biosensor's ability to detect Troponin I with high sensitivity and specificity. The impedance spectra show that the biosensor can detect Troponin I at concentrations ranging from 100 attomolar (aM) to 100 picomolar (pM), with a detection limit of 100 aM. The biosensor exhibits a linear response to increasing Troponin I concentrations, confirming its potential for practical applications in AMI detection. The study also highlights the stability and repeatability of the biosensor. The 3D LSG_MoS_2_Ag NPs hybrid maintains its performance over multiple cycles, with a high degree of stability and reproducibility. The biosensor's stability is further tested over six weeks, showing an 87% retention in performance, indicating its suitability for long-term use [140].

2.3.5 MoS_2/RGO hybrids prepared by a hydrothermal route as a highly efficient catalytic for sonocatalytic degradation of methylene blue

The paper details the synthesis and application of MoS_2/reduced graphene oxide (RGO) hybrids as efficient sonocatalysts for the degradation of methylene blue (MB). The focus is on the enhanced catalytic performance due to the unique hierarchical structure of the MoS_2/RGO hybrids, which was achieved through a one-pot hydrothermal method. The synthesis process begins with the preparation of graphene oxide (GO) from natural graphite powder using a modified Hummers' method. This involves mixing graphite powder with sodium nitrate and sulfuric acid in an ice bath, followed by the gradual addition of potassium permanganate. The mixture is then heated, and after adding hydrogen peroxide and hydrochloric acid, the solution is centrifuged to obtain the GO, which is subsequently dried to form a powder. Nanosized MoS_2 is synthesized by mixing thiourea and ammonium molybdate in deionized water to form a dispersion solution. This solution is placed in a Teflon-lined stainless-steel autoclave and heated at 200°C for 24 hours. The resulting product is washed and dried to yield nanosized MoS_2. For the MoS_2/RGO hybrids, varying amounts of GO powder are dispersed in deionized water using ultrasonic treatment. Thiourea and ammonium molybdate are then added to this solution, and the mixture is subjected to the same hydrothermal conditions as the MoS_2 synthesis. This results in MoS_2 nanosheets anchored onto the RGO, forming a hierarchical structure that prevents the undesirable stacking of MoS_2 layers.[141] Characterization techniques such as SEM, TEM, XRD, XPS, and Raman spectroscopy confirm the successful synthesis of MoS_2/RGO hybrids. The SEM and TEM images show well-dispersed MoS_2 nanoflowers on both sides of the RGO, indicating a significant increase in active sites for catalytic reactions. XRD patterns reveal the expansion of MoS_2 interlayer spacing due to GO insertion, enhancing electron conductivity and light absorption. Raman spectroscopy confirms the strong interaction between MoS_2 and RGO, while XPS analysis indicates the successful reduction of GO to RGO during synthesis. The sonocatalytic performance of the MoS_2/RGO hybrids is evaluated through the degradation of MB under ultrasonic irradiation. The results show that MoS_2/RGO hybrids exhibit significantly higher catalytic activity than pure MoS_2. This enhanced performance is attributed to the hierarchical structure, which promotes efficient electron-hole separation and increases the availability of reactive sites. The study also investigates the effects of various parameters on the sonocatalytic degradation efficiency, including catalyst dosage, initial MB concentration, pH, and ultrasonic power. It is found that increasing the catalyst dosage improves degradation efficiency, while higher initial MB

concentrations reduce it. The optimal pH for degradation is found to be 9, and higher ultrasonic power enhances catalytic performance by generating more reactive radicals.

2.3.6 Clean energy by using $NiCo_2O_4/MoS_2$ nanocomposites prepared by hydrothermal method

The paper discusses the synthesis, characterization, and performance of $NiCo_2O_4/MoS_2$ nanocomposites for photocatalytic applications, focusing on hydrogen production from water under visible light. The development and industrial activities have led to increased emissions of toxic and harmful gases, threatening ecological and environmental safety. These gases, including automobile exhaust and industrial waste gases, not only harm human health but also contribute to phenomena like acid rain [142]. Consequently, improving the detection and control of these emissions is crucial. Traditional semiconductor materials such as TiO_2 have limited responses to sunlight, restricting the development and application of photocatalytic technology. To address this, the study explores the synthesis of $NiCo_2O_4/MoS_2$ nanocomposites via the hydrothermal method to enhance photocatalytic performance. This composite aims to improve the utilization of visible light and the efficiency of hydrogen production through water photolysis. Molybdenum disulfide (MoS_2) nanorods were synthesized using a solvothermal method. Initially, 4.66 g of $Mo(NO_3)_2 \cdot 4H_2O$ and 3.45 g of thiourea were dissolved in 70 mL of ethylenediamine and mixed for 30 minutes at room temperature. The mixture was then transferred to a high-pressure reactor and heated at 160°C for 24 hours. After cooling to room temperature, the product was washed with deionized water and anhydrous ethanol, followed by drying at 60°C for 8 hours. For the preparation of $NiCo_2O_4/MoS_2$ nanocomposites, MoS_2 was dispersed in deionized water and mixed with a solution of $Mo(NO_3)_2 \cdot 4H_2O$ and $Na_2WO_4 \cdot 4H_2O$. After adding NH_4F and stirring for 30 minutes, the mixture underwent a process similar to that used for MoS_2 synthesis. The composites were prepared with different mass ratios of $NiCo_2O_4$ to MoS_2 and labelled as 1.2-$NiCo_2O_4/MoS_2$, 1.4-$NiCo_2O_4/MoS_2$, and 1.6-$NiCo_2O_4/MoS_2$ [143].

The $NiCo_2O_4/MoS_2$ composites were characterized using X-ray diffraction (XRD), scanning electron microscopy (SEM), transmission electron microscopy (TEM), and energy-dispersive X-ray spectroscopy (EDS). The XRD patterns confirmed the formation of the composites, showing diffraction peaks corresponding to $NiCo_2O_4$ and monoclinic MoS_2. SEM and TEM images revealed the rod-like structure of MoS_2 and the granular morphology of $NiCo_2O_4$, with $NiCo_2O_4$ nanoparticles uniformly distributed on the MoS_2 rods. EDS analysis confirmed the

presence of elements such as O, W, Zn, S, and Mo in the composite. The photocatalytic activity of the composites was evaluated by measuring their hydrogen production rates from water photolysis under visible light. The 1.4-$NiCo_2O_4/MoS_2$ composite exhibited the highest hydrogen production rate of 79.27 mmol/h/g, significantly higher than that of pure MoS_2 (1.21 mmol/h/g) [143]. This enhancement was attributed to the efficient separation and migration of photogenerated carriers facilitated by the composite structure. The stability of the composites was confirmed through cyclic hydrogen production experiments, showing no significant inactivation. To further understand the photocatalytic mechanism, free radical capture experiments were conducted. The results indicated that superoxide radicals ($\cdot O^{2-}$) were the main active species responsible for the photocatalytic activity. The photogenerated electrons from MoS_2 were effectively transferred to $NiCo_2O_4$, where they reacted with H+ to produce H_2. This separation of photogenerated carriers prevented recombination, enhancing the photocatalytic efficiency. The study successfully synthesized $NiCo_2O_4/MoS_2$ composites via the hydrothermal method, demonstrating significant improvements in photocatalytic hydrogen production under visible light. The composites showed enhanced stability and efficiency compared to pure MoS_2. However, the study was conducted in a laboratory setting with a small sample size, suggesting the need for further research to evaluate the composites' performance in real-world applications.

2.3.7 Hydrothermal Synthesis and Electrochemical Properties of MoS_2/C Nanocomposite

The research paper discusses the synthesis, characterization, and electrochemical properties of a molybdenum disulfide/carbon (MoS_2/C) nanocomposite, with a focus on its application as an anode material for sodium-ion batteries (SIBs). The motivation behind this study is to find an alternative to lithium-ion batteries (LIBs) due to the abundant and low-cost nature of sodium. However, the larger ion radius and transport barrier of sodium restrict the choice of electrode materials for SIBs. Transition metal dichalcogenides, such as molybdenum disulfide (MoS_2), have garnered attention due to their layered structure, which is similar to graphite, and their potential as anode materials for sodium-ion storage. MoS_2's structure consists of layers of molybdenum atoms sandwiched between sulfur atoms, held together by van der Waals forces, allowing sufficient space to host sodium ions. Despite its high theoretical specific capacity and good cycling performance, MoS_2 suffers from poor electronic and ionic conductivity, large volume expansion, and pulverization when used as an anode, leading to poor cycle performance

and rate capability. To address these issues, they designed a MoS_2/C composite by incorporating conductive carbon to enhance electronic and ionic conductivity and buffer the volume expansion during charge-discharge processes. The composite was synthesized using a simple hydrothermal method, where sodium molybdate, thiourea, and glucose were dispersed in ultrapure water, stirred, and then hydrothermally treated at 180°C for 24 hours. The resulting product was then carbonized at 800°C for 2 hours under an argon atmosphere [144]. Characterization of the synthesized MoS_2/C composite was performed using X-ray diffraction (XRD), field-emission scanning electron microscopy (FESEM), high-resolution transmission electron microscopy (HRTEM), and Raman spectroscopy. These analyses revealed that the MoS_2/C composite had a flower-like particle structure with wrinkled nanosheets coated with a carbon layer, and it displayed enhanced electrochemical properties compared to pristine MoS_2. The electrochemical performance of the MoS_2/C composite was evaluated using two-electrode cells versus metallic sodium. The composite exhibited an initial capacity of 475.1 mAh g^{-1} at a current density of 100 mA g^{-1} and maintained 71% of its initial capacity after 100 cycles at 250 mA g^{-1}. This improvement is attributed to the conductive carbon, which suppressed significant volumetric changes in MoS_2 during the charge/discharge process and increased its electrical conductivity [144].

2.3.8 MoS_2−Ag Nanocomposite-Based SERS Substrates with an Ultralow Detection Limit

The paper explores the synthesis, characterization, and application of a MoS_2-Ag nanocomposite for surface-enhanced Raman spectroscopy (SERS) substrates with an ultralow detection limit. The use of two-dimensional (2D) materials in SERS is driven by their electronic properties, tunable band gap, and layered structure with high absorption power. Molybdenum disulfide (MoS_2) has been a focal point in this regard due to its robustness, natural abundance, and significant chemical activity. Various morphologies of MoS_2, such as nanosheets, nanorods, nanoplates, and nanoflowers, have been synthesized using different methods, with hydrothermal synthesis being particularly effective for achieving the desired morphological variations. The study focuses on the synthesis of different MoS_2 morphologies and their subsequent functionalization with Ag nanoparticles (NPs) to enhance their SERS performance, particularly for detecting RhB dye molecules. The MoS_2 and MoS_2-Ag nanocomposites were synthesized using a hydrothermal method. Initially, ammonium molybdate tetrahydrate and thiourea were mixed in deionized water and stirred until a blue color appeared. The solution

was then transferred to a Teflon-lined autoclave and heated at 180°C for 18 hours to obtain flower-like MoS_2. For interconnected-nanoplate MoS_2, the reaction time was increased to 36 hours, resulting in less stacking and thinner structures. For nanosheet MoS_2, a mixture of dimethylformamide (DMF) and deionized water was used as a solvent, and the reaction time was extended to 48 hours. The nanosheets obtained were uniform and ultrathin. Ag NPs were then decorated on the MoS_2 nanoplates by chemically reducing $AgNO_3$ in the presence of MoS_2 to form the MoS_2-Ag nanocomposite [145]. The morphological features of the synthesized materials were analyzed using SEM, FESEM, and TEM. The flower-like MoS_2 showed smooth surfaces and clear boundaries, while the interconnected nanoplates and nanosheets displayed less stacking and thinner structures. UV-visible spectroscopy revealed broad absorption spectra in the visible region for all MoS_2 morphologies. XRD and Raman spectroscopy confirmed the structural characteristics of the different MoS_2 morphologies and the successful formation of the MoS_2-Ag nanocomposite. The SERS performance of the MoS_2 and MoS_2-Ag substrates was evaluated using RhB dye as a probe molecule. The interconnected-nanoplate MoS_2 exhibited the best SERS response, detecting RhB concentrations as low as 10^{-9} M. The MoS_2-Ag nanocomposite further enhanced the SERS signal, achieving an ultralow detection limit of 10^{-15} M for RhB dye [145]. The enhancement was attributed to the combined effects of electromagnetic and chemical mechanisms. The presence of Ag NPs created localized surface plasmon resonance (LSPR), which enhanced the electric field and facilitated charge transfer between MoS_2 and RhB molecules. The study successfully synthesized various morphologies of MoS_2 and functionalized them with Ag NPs to form MoS_2-Ag nanocomposites. The interconnected-nanoplate MoS_2-Ag nanocomposite exhibited the best SERS performance, with an ultralow detection limit for RhB dye. This work demonstrates the potential of MoS_2-Ag nanocomposites as effective SERS substrates for detecting low concentrations of harmful dyes and other molecules, offering significant advantages for environmental monitoring and biosensing applications. Further research is needed to optimize the synthesis process and explore the practical applications of these nanocomposites.

2.3.9 Characterizations of synthesized laser-scribed graphene/ molybdenum disulfide (LSG/MoS_2) hybrids for supercapacitor performance

The article discusses the development of a sustainable and organic energy storage system using oil palm lignin waste-derived laser-scribed graphene (LSG) embedded with molybdenum disulfide (MoS_2). This hybrid material, referred to as LSG/MoS_2, aims to address the zero-band

gap issue of graphene, the restacking problem of molybdenum disulfide, and to enhance electrical conductivity. To synthesize the LSG/MoS_2 hybrids, various amounts of LSG (0.1, 0.5, and 1.0 grams) were added to a MoS_2 precursor, and a nanoscale LSG/MoS_2 hybrid nanostructure was produced via the hydrothermal method. Raman spectroscopy confirmed the formation of graphene from lignin by identifying the characteristic D, G, and 2D bands of LSG. The morphological analysis using FESEM revealed a porous structure with a large surface area, anchored with 3D MoS_2 nanoflowers. TEM imaging further demonstrated the decoration of LSG with MoS_2, showing a lattice spacing corresponding to the (002) and (100) planes of MoS_2 [146]. The synthesis process began with the preparation of lignin-based graphene through a laser scribing technique. A 20% lignin solution was created by dissolving lignin powder in distilled water and stirring it until homogeneous. This solution was then drop-coated onto a glass substrate, dried, and subjected to CO_2 laser scribing to transform the lignin into graphene. The modified LSG, which included carbon black to enhance conductivity, was then prepared [146] For the fabrication of LSG/MoS_2, 0.1 grams of modified LSG, 0.6 grams of sodium molybdate dehydrate, and 1.77 grams of thiourea were dissolved in distilled water. This mixture was stirred and then subjected to the hydrothermal process at 200°C for 24 hours, resulting in black precipitates of LSG/MoS_2. The precipitates were washed and dried, and the procedure was repeated with different amounts of LSG to create varying hybrid concentrations. Electrochemical performance tests, including Electrochemical Impedance Spectroscopy (EIS), Cyclic Voltammetry (CV), and Galvanostatic Charge Discharge (GCD), revealed that LSG with 0.1 grams of MoS_2 exhibited the lowest resistance, the highest specific capacitance of 6.7 mF/cm^2 at 0.05 mA/cm^2, and excellent cyclic stability of 98.1% over 1000 cycles. The EIS results showed reduced transfer resistance and enhanced redox reactions, while the CV and GCD tests demonstrated superior capacitive behavior and cyclic stability, particularly for the LSG/MoS_2-1.0 hybrid [146].

2.3.10 Hydrothermal Synthesis of MoS_2/SnS_2 Photocatalysts with Heterogeneous Structures Enhances Photocatalytic Activity

The study focuses on the synthesis and evaluation of MoS_2/SnS_2 photocatalysts with heterogeneous structures, aiming to enhance photocatalytic activity for degrading organic pollutants. This is a promising strategy to address pollution and energy crises by utilizing solar photocatalysis. The synthesis of the MoS_2/SnS_2 composite catalysts was achieved through a hydrothermal method. Initially, MoS_2 nanoparticles were synthesized by dissolving 1.0592 g

of ammonium molybdate tetrahydrate and 1.828 g of thiourea in 60 mL of deionized water. This solution was transferred to a Teflon-lined autoclave and heated at 180°C for 16 hours. The resulting black precipitate was dried at 80°C for 2 hours [147]. For the preparation of the MoS_2/SnS_2 composite catalysts, the MoS_2 powder was dispersed in 60 mL of deionized water to form a suspension. $SnCl_4 \cdot 5H_2O$ and CH_4N_2S were added to the suspension, followed by the addition of hydrochloric acid to adjust the acidity. The mixture was then transferred to a Teflon-lined autoclave and heated at 180°C for various reaction times (12, 14, and 16 hours). The catalysts were collected by centrifugation and dried at 80°C for 2 hours. The final catalysts were named based on the reaction time and molar ratio of molybdenum to tin, such as MS12-2-H, MS14-2-H, and MS16-2-H. Electrochemical impedance measurements indicated that the charge transfer resistance of the composite catalysts decreased with reaction time, improving photocatalytic degradation performance. The photocatalytic activity was evaluated by degrading methylene blue (MB) under visible light. The MS14-2-H catalyst exhibited the highest degradation rate of 83% after 80 minutes of irradiation, followed by MS12-2-H with 55.9%. The degradation performance was consistent with the structural and electrochemical properties, confirming the optimal reaction conditions for the synthesis of the composite catalysts [147].

2.3.11 $Fe_3O_4@MoS_2$/RGO as an effective nano-electrocatalyst toward electrochemical hydrogen evolution reaction and methanol oxidation in two settings for fuel cell application

The study investigates the synthesis and application of a three-component nano-electrocatalyst, $Fe_3O_4@MoS_2$/RGO, designed to enhance the efficiency of the electrochemical hydrogen evolution reaction (HER) and methanol oxidation reaction (MOR) in fuel cell applications. This catalyst comprises magnetite (Fe_3O_4) coated with molybdenum disulfide (MoS_2) and hybridized with reduced graphene oxide (RGO). The study evaluates its performance in both acidic and alkaline media, providing insights into its potential as a substitute for platinum-based catalysts. The synthesis of the $Fe_3O_4@MoS_2$/RGO nanocatalyst involved a two-step hydrothermal method. Initially, graphene oxide (GO) was synthesized using a modified Hummer's method. This involved the oxidation of graphite powder with sulfuric acid, sodium nitrate, and potassium permanganate, followed by sonication and washing to produce GO. The GO was then reduced to RGO by treating it with ammonia and hydrazine hydrate under reflux conditions [148]. To prepare the $Fe_3O_4@MoS_2$/RGO nanocatalyst, MoS_2, and Fe_3O_4

nanoparticles were first synthesized separately according to established methods. MoS_2 nanoparticles were produced by reacting sodium molybdate with thioacetamide, while Fe_3O_4 nanoparticles were synthesized by co-precipitating iron(III) chloride and iron(II) sulfate with ammonia. These nanoparticles were then combined with RGO in a hydrothermal reactor at 240°C for 24 hours, yielding the Fe_3O_4@MoS_2/RGO composite. The electrochemical performance of the Fe_3O_4@MoS_2/RGO catalyst was evaluated using cyclic voltammetry (CV), linear sweep voltammetry (LSV), and chronoamperometry. In alkaline media, the catalyst exhibited high activity for methanol oxidation, with the optimal methanol concentration identified as 0.3 M. The addition of RGO enhanced the charge transfer rate and increased the surface area for methanol adsorption, leading to improved catalytic performance. The presence of porous MoS_2 provided additional active sites for electron transfer, further boosting the catalytic activity. In acidic media, the Fe_3O_4@MoS_2/RGO catalyst also demonstrated effective methanol oxidation and hydrogen evolution. The Tafel slope for HER was measured at 48 mV dec^{-1}, indicating a favorable kinetic performance. The synergistic effect between Fe_3O_4 and MoS_2, along with the conductive properties of RGO, contributed to the enhanced electrocatalytic activity and stability of the catalyst [148].

2.4 Literature review on Dye degradation

2.4.1 Sunlight-driven MoS_2 nanosheets mediated dye degradation

Due to increased industrialization, dumping of untreated hazardous organic pollutants directly into water bodies has led to water pollution. It has become necessary to detect and degrade toxic organic compounds. Photocatalysis process using MoS_2 can be used for this purpose. Layered transition metal dichalcogenide (LTMD) MoS_2 has strong covalent bonding between Mo and S, as well as Van der Waals forces in between the layers [149], giving rise to excellent electronic and optical properties. The pristine MoS_2 nanosheets have shown great photocatalytic activity towards the CV dye due to low bandgap energy, high surface-to-volume ratio, and multiple active edge sites [150]. MoS_2 nanosheets are prepared by facile hydrothermal route in an argon atmosphere kept at 200°C for 24 h. The flake-like structure of MoS_2 is formed with 5-6 layers that can be successfully used as a catalyst to decompose crystal violet dye.

2.4.2 Degradation of mixed dye pollutants by integrated adsorption-photocatalysis technique

MoS_2 is an LTMD that can be used to design a heterojunction catalyst and its dye removal performance relies on its crystalline phase (2H/1T), and surface charge potential [151]. In addition to being semiconducting photocatalysts, MoS_2 has excellent adsorption properties as well due to its high surface area and abundant active sites [152]. However, MoS_2 shows a high affinity for anionic dye, which limits its use in mixed dye pollutants. Adsorbent properties of MoS_2 are explored in an integrated approach to remove cationic and anionic pollutants together by harnessing both adsorption and photocatalytic properties. The study investigates the synthesis of MoS_2/TiO_2 nanocomposites with varying weight percentages of MoS_2 (2.5%, 5%, 10%, 20%, 30%, and 50%) using a two-step hydrothermal method. The two-stage process involves using a high weight percentage of MoS_2 (50%) in Stage I for dark mode adsorption and a low weight percentage of MoS_2 (2.5%) in Stage II for light-irradiated photocatalysis. This method demonstrated the complete removal of methylene blue dye at a rate five times faster than conventional single-stage treatments. The results can be attributed to the widened lattice spacing in 2D MoS_2 nanostructure which enhances dye adsorption, and the effective charge separation at the MoS_2/TiO_2 heterojunctions, facilitating photocatalytic degradation. This MoS_2/TiO_2 nanocomposite can be used successfully in real-world applications like wastewater treatment.

2.4.3 Rapid degradation of Rhodamine B under concentrated sunlight irradiation

Due to rapid industrialization and unplanned urbanization, water pollution has become a global problem and such, finding a sustainable cost-effective wastewater treatment process is an immediate necessity. For a few decades, wide-bandgap semiconductor photocatalysts have been studied extensively for photocatalytic wastewater treatment [153]. MoS_2 has attracted attention as a photocatalyst due to its high mobility of charge carriers and excellent optical absorption properties [154]. Moreover, MoS_2 can be easily synthesized on a large scale by cost-effective hydrothermal methods [155]. Despite much research to increase photocatalytic activity, no technique has been applied to utilize sunlight for wastewater treatment. A new technology for concentrated sunlight-driven photocatalytic wastewater treatment of MoS_2 nanoflowers has been reported where a solar concentrator coupled with an optical fiber bundle

has been used to deliver concentrated sunlight to the photocatalytic reactor, achieving irradiance power 2.6 times higher than ordinary sunlight [156]. The MoS_2 nanoflowers, prepared via a simple hydrothermal method, exhibited a significant photocatalytic activity, facilitating the degradation of Rhodamine B (RhB) dye by 67.4% in 120 minutes, which is 1.7 times faster than under ordinary sunlight. This research opens new avenues for sustainable and cost-effective wastewater treatment technologies utilizing solar energy.

2.4.4 Layered MoS_2 for photocatalytic dye degradation

MoS_2 is an important TMD that can be used in photocatalytic dye degradation processes. Photocatalytic degradation of methylene blue (MB) and crystal violet (CV) dyes using layered MoS_2 nanostructures have been studied where the nanostructures were synthesized via a hydrothermal reaction with Lawesson's reagent (LR) as the sulfur source. The MoS_2 nanostructures were formed after a 15-hour reaction at 120°C and characterized. The study found that MoS_2 effectively degraded MB and CV dyes under both natural sunlight and artificial UV light. Under natural sunlight, the MoS_2 photocatalyst degraded 71% of MB and 57% of CV within 90 minutes. When exposed to an artificial UV lamp, the degradation efficiency increased to 82% for MB and 73% for CV. The enhanced photocatalytic activity under UV light is attributed to the higher energy of UV photons, which increases electron-hole pair generation, leading to more effective dye degradation. The proposed synthesis method can also be used to synthesize other metal sulfides [157].

2.4.5 Photocatalytic Degradation of Methyl Orange using MoS_2 nanoparticles as catalyst

MoS_2, a semiconductor transition metal dichalcogenide material, exhibits promising optoelectronic properties due to its band gap energy falling within the visible light range. MoS_2, being nontoxic, can be used as a good material to degrade such dye by using solar energy through a photocatalytic activity which is an eco-friendly and cheaper way [158]. In this study, MoS_2 NPs have been synthesized to investigate the photocatalytic behavior of methyl orange (MO) as a model dye [159]. The authors synthesized MoS_2 NPs through a solid-state reaction involving molybdic acid and thiourea under nitrogen gas at 500°C. The photocatalytic activity was assessed by degrading a 10μM MO solution under visible light irradiation. Results showed that MoS_2 NPs efficiently degraded MO, achieving 98% degradation with 1mg/ml catalyst

concentration in 2 hours. This efficiency is attributed to the broad absorption of visible light by the MoS_2 NPs, which generate electron-hole pairs (excitons) that react with water and oxygen to produce hyperactive hydroxyl ions. These ions further degrade the MO dye molecules. MoS_2 NPs have the potential as an eco-friendly and reusable photocatalyst for degrading toxic dyes in industrial wastewater, thus preventing environmental pollution. The catalyst's reusability and stability further enhance its practical application, making the photocatalytic process cost-effective and advantageous for large-scale implementation.

2.4.6 Green synthesis of MoS_2 for degrading MB and CV under natural sunlight

MoS_2 is a typical 2D LTMD that has garnered interest as a catalyst in dye degradation applications owing to its narrow band gap, high visible light absorption, low toxicity, and more active sites [160]. The preparation of layered MoS_2 nanosheets has become a major challenge and most of the existing MoS_2 nanosheets are synthesized using more than two steps [161]. A novel green synthesis of MoS_2 nanoflowers has been reported by using ammonium molybdate and thiourea as the molybdenum and sulfur source by using a hydrothermal method without using any acids or bases. The synthesis process involves a fast nucleation, fusion, and Ostwald ripening [162] that results in MoS_2 NFs with a good crystallinity and a lattice spacing. The study demonstrates the photocatalytic efficiency of the MoS_2 NFs under natural sunlight by degrading MB and CV dyes. The results showed nearly 100% degradation of both dyes, which is reported as the fastest degradation rate under stirring conditions. This high efficiency is attributed to the low bandgap, layered structure, abundant edge sites, and high surface area of the MoS_2 NFs. The MoS_2 NFs also exhibited excellent stability over multiple cycles of use. This study presented a simple, green synthesis method for MoS_2 nanoflowers with exceptional photocatalytic properties, offering a promising approach for the degradation of organic pollutants under natural sunlight.

2.4.7 Photocatalytic Dye Degradation by MoS2 NS synthesized by different routes

Though hydrothermal synthesis of MoS_2 is cost-effective, fast, easy, and serves many purposes, it forms an uncontrolled number of layers and nonuniform morphology with poor crystallinity that affects the fabrication of quickly modulated optical devices for practical applications [163]. Liquid-based sonication-assisted exfoliation offers better control over the number of layers and maintains uniformity, resulting in improved crystallinity and potentially enhanced photocatalytic response. However photocatalytic activity of MoS_2 generated by this method

has not been explored much with respect to the degradation of dyes. Thus, both the hydrothermal and the liquid-sonication methods was studied to explore the effect of synthesis routes on the photocatalytic application of MoS_2 NSs for the degradation of organic dyes MR and MB. The results show that MoS_2 NSs synthesized via hydrothermal methods exhibit moderate photocatalytic activity, achieving degradation efficiencies of 58.92% for MR and 49.28% for MB under visible light irradiation. In contrast, NSs synthesized through liquid-phase exfoliation demonstrate higher efficiencies, with degradation rates of 63.40% for MR and 62.40% for MB [164]. The enhanced performance is attributed to the better crystallinity and increased reactive edge sites provided by the liquid-exfoliated NSs. The superior performance of sonication-based synthesis suggests it to be a promising alternative for the generation of MoS_2 that can be further applied in large-scale industries.

2.4.8 Sodium dodecyl sulfate mediated hydrothermal synthesis of MoS_2 NSs

Synthesis of MoS_2 nanosheets (NSs) using sodium dodecyl sulfate (SDS) and their applications in photocatalytic dye degradation and dye-sensitized solar cells (DSSCs) is investigated. SDS-assisted hydrothermal synthesis produces well-defined MoS_2 nanosheets with enhanced stability and dispersion. This method is cost-effective and efficient, making it suitable for large-scale applications. The MoS_2-SDS NSs exhibit excellent photocatalytic activity, effectively degrading organic dyes like Methylene Blue (MB) under light irradiation by generating reactive oxygen species from electron-hole pairs [165]. In DSSC applications, MoS_2-SDS NSs serve as effective counter-electrode materials, demonstrating promising power conversion efficiency (PCE). The incorporation of SDS improves both the dispersion and catalytic activity of the nanosheets, enhancing the overall performance of DSSCs. This research highlights the versatility and effectiveness of SDS-mediated hydrothermal synthesis of MoS_2 nanosheets, showcasing their potential in environmental and energy applications. The dual functionality in photocatalysis and DSSCs underscores the broad applicability and multifunctional capabilities of these nanosheets in sustainable technologies.

2.5 Objectives

The primary objective of this study is to fabricate a MoS_2-based nanocomposite using a one-pot hydrothermal route to enhance dye degradation performance under visible light.

The specific objectives are

- Process optimization for the preparation of MoS_2 nanomaterial through a one-pot hydrothermal route
- Selection of additives to aid in the synthesis of MoS_2 with improved structural stability and geometry to promote the generation of electron-hole pairs under sunlight
- Characterization of the prepared nanomaterials
- To study the efficacy of the prepared MoS_2 as a photocatalyst for the degradation of a cationic dye, Malachite Green dye under visible light.
- Optimization of the process conditions for dye removal
- To study the kinetics of the photodegradation of malachite green using MoS_2 as photocatalyst

3 Experimental Methods

3.1 Experimental Design

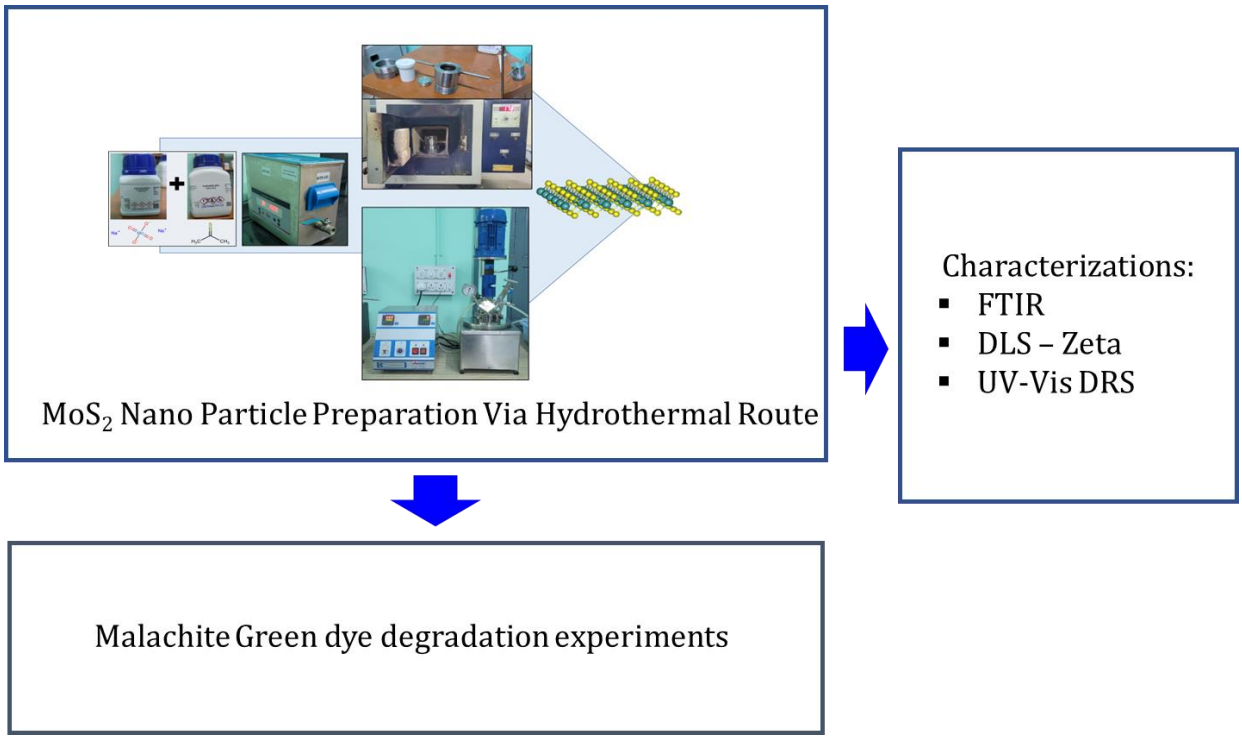


Figure 2: Experimental Design

3.2 Materials & Methods

All the chemicals used in the work were of analytical grade and used without further purification. Sodium molybdate ($Na_2MoO_4 \cdot 2H_2O$ with 99% purity), thiourea (CH_4N_2S with 99% purity), ethanol, HCL, Citric acid, HNO_3, H_2SO_4 & Malachite green was purchased from Merck. A stainless-steel autoclave hydrothermal reactor with a Teflon seat was supplied from AMAR instruments.

3.3 Hydrothermal synthesis of MoS_2 nanomaterials

Sodium Molybdate ($Na_2MoO_4 \cdot 2H_2O$) and Thiourea (CH_4N_2S) were dissolved in deionized water (DI water) (60 mL) and sonicated for 30 min, then additives like HCL, Citric acid, HNO_3, H_2SO_4 and NaOH was added into the mixture. The mixture was then transferred into a Teflon seat inside a hydrothermal stainless-steel autoclave (100 mL) reactor consisting of a rotator and maintained at varying temperatures of 160°C, 180°C, and 200 °C for varying amounts of time. After the mixture cooled to room temperature, the products were collected by centrifugation and washed with DI water and ethanol three times respectively, followed by drying at 60 °C for 12 h in a hot air oven and the final products were collected as seen in Fig 1. Dye degradation tests and characterizations were carried out using the same products. The samples prepared have been termed using the run no. as seen in Table 4.

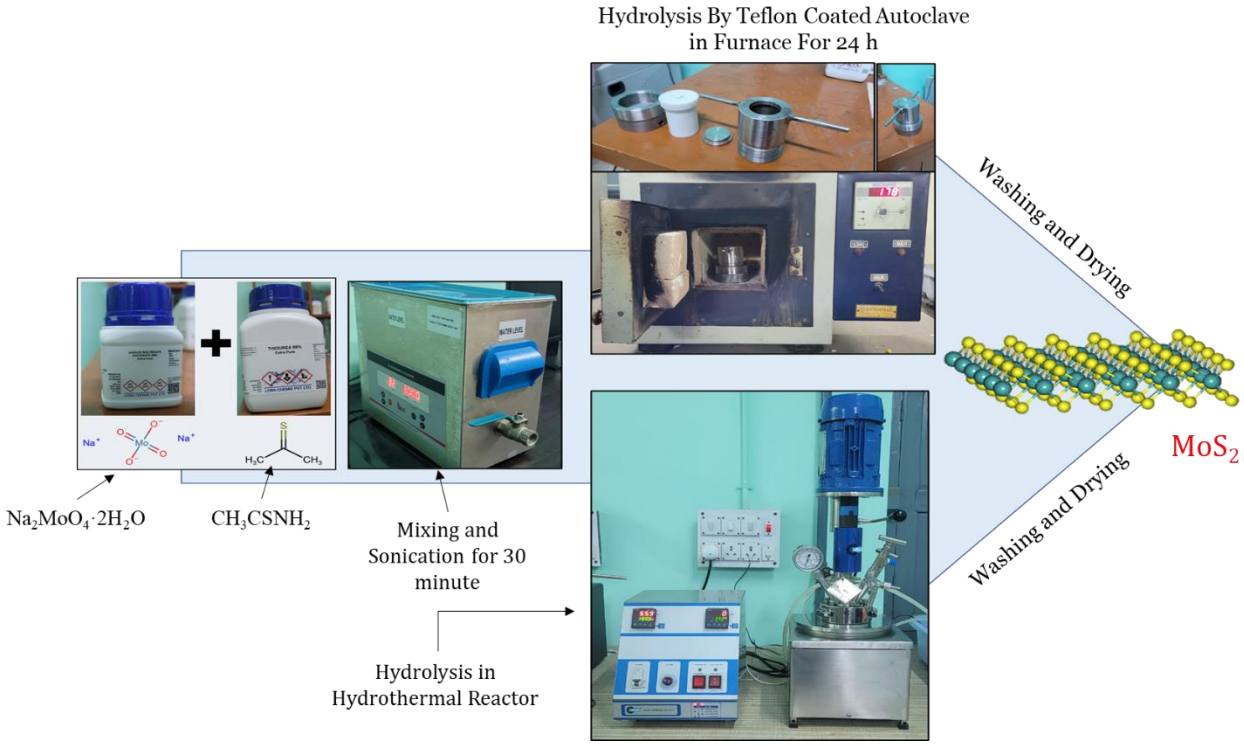


Figure 3: Preparation of MoS_2

Table 4: MoS_2 samples prepared under varying conditions

Run	Precursors (gram)		Additional Chemicals (ml)		Sonication (Min)	Solution (ml)	Pressure (bar)	Parameters in hydrothermal route			Material (gram)	Yield (%)
	Sodium Molybdate	Thiourea	3M HCl	3M NaOH				Temp. (°C)	Time (H)	RPM		
1	0.723	1.14	NA	NA	30	60	10	180	24	700	**0.069**	**9.5**
2	1.45	2.28	NA	NA	30	60	10	180	24	700	**0.317**	**21.8**
3	1.45	2.28	6.1	NA	30	60	10	180	24	700	**0.793**	**54.7**
4	1.45	2.28	NA	5.5	30	60	10	180	24	700	**0.472**	**32.5**
5	1.45	2.28	NA	NA	30	60	16.5	200	24	700	**0.708**	**48.8**
6	1.45	2.28	6.1	NA	30	60	16	200	24	700	**1.042**	**71.8**
7	0.723	1.14	6	NA	30	60	15.5	200	24	700	**0.565**	**78**
8	2.9	4.56	13	NA	30	60	22	200	24	700	**1.66**	**57**
9	0.723	1.14	4(3M HNO_3)	NA	30	60	15	200	24	700	**0.08**	**11**
10	1.45	2.28	2(1M H_2SO_4)	NA	30	60	20	200	24	700	**0.964**	**66.5**
11	0.723	1.14	30(1M Ascorbic acid)	NA	30	30	22	200	24	700	-	-
12	1.45	2.28	5.5(3M HNO_3)	NA	30	60	17	200	24	700	**0.598**	**41**
13	1.45	2.28	10(1M Ascorbic acid)	NA	30	60	20	200	24	700	**1.034**	**71.3**
14	0.723	1.14	NA	NA	30	60	7	160	25	700	**0.032**	**4.42**
15	1.45	2.28	NA	NA	30	60	7	160	24	700	**0.150**	**10.3**
16	0.723	1.14	6	NA	30	60	7.5	160	24	700	**0.386**	**53.4**

3.4 Dye Degradation Experiments

The photocatalytic oxidation of malachite green (MG) in MoS_2 suspension under ambient sunlight was investigated to evaluate the photocatalytic dye degradation capability of the prepared MoS_2 nanoparticles. malachite green (MG) was chosen as the model dye for the photodegradation experiments. Samples with the highest yield for each condition of temperature, the ratio of precursors, and additional chemicals during synthesis were selected for dye degradation experiments considering the economic implications of synthesis, dye stock was prepared by adding specified quantities of MG dye to DI water In a typical experiment 0.1g MoS_2 was added under stirring to 10ml of 50mg/L MG dye at neutral pH in glass

containers and kept in dark for 30min to establish the adsorption equilibrium before it was introduced to ambient sunlight for two hours. The samples with the best degradation (Run No. 3, 6,7,10, and 13) were then tested for degradation capacity at varying pH. Upon, identifying the best combination of pH and sample (identified as Run No. 7 at pH 6), catalyst loading was also varied to obtain the optimum MoS_2 loading necessary (identified as 1g/L of dye solution), further dye concentration was varied to obtain details about the kinetic parameters of photocatalysis. Operating parameters such as catalyst loading, dye concentration and time were varied to investigate their effects on the photocatalytic activities of prepared photocatalysts. A similar set of experiments was carried out under a UV lamp to check the performance under the UV spectrum. Degradation was measured using a UV-Vis spectrophotometer, and the kinetic parameters were analyzed.

3.5 Characterizations of prepared Nanomaterials

Several techniques were employed for the characterization of the samples. FTIR (Jasco) was mainly used as a qualitative technique for the study of the surface chemical functional groups on MoS_2 nanoparticles. During FTIR analysis, the prepared sample was directly introduced to the instrument. To determine the crystal phase composition and the crystallite size of the photocatalysts. The UV-Vis diffuse reflectance spectra (DRS) were measured using a UV-Vis spectrophotometer (Perkin Elmer LAMDA 950) with an integrating sphere attachment and $BaSO_4$ was used as the reference to obtain the band gap of the prepared MoS_2. A DLS-Zeta instrument (Malvern Zetasizer) was used to obtain the particle size and surface charge data. The samples were suspended in an aqueous solution at a concentration of 0.01% and sonicated before being analyzed.

4 INSTRUMENTS AND APPARATUS

4.1 UV-Vis Diffuse Reflectance Spectroscopy

In DRS, the Kubelka–Munk function was used to conduct band gap analysis. The K–M theory is based on a continuum model (Fig. 16), where the reflectance properties for infinitesimally small layers are described by differential equations [112]. Here, the letters I and J represent radiations in the downward and the upward direction, respectively. The downward flux through a layer of thickness dx is decreased by absorption and scattering

processes and increased by the scattering process of the light traveling upward towards the surface [113]. Originally, a model is known as the K-M model was used to describe the behavior of light traveling inside a light-scattering specimen, which is based on the following differential equations:

-di = -(S+K) i dx + S jdx

dj = -(S+K) j dx + S idx

where i and j are the intensities of light traveling inside the sample towards its un-illuminated and illuminated surfaces, respectively; dx is the differential segment along the light path; S and K are respectively called as „K–M scattering" and „absorption" coefficients. The last two quantities (S and K) have no direct physical meaning on their own, even though these appear to represent the respective portions of scattered and absorbed lights, per unit vertical length. K–M model holds well when the particle size is comparable to, or smaller than the wavelength of the incident light. In such a situation the diffuse reflection no longer allows to separate the contributions of the reflection, refraction, and diffraction, implying that scattering takes place. In the limiting case of an infinitely thick sample, the thickness and sample holder have no influence on the value of reflectance (R). In this case, the K–M equation becomes

Kubelka-Munk Function: $\frac{K}{S} = \frac{(1-R_\infty)^2}{2R_\infty} = F(R_\infty)$

F(R∞) is the so-called remission or Kubelka–Munk function, where R∞ =R_{sample}/ $R_{standard}$. For parabolic band structure, the band gap (Eg), and absorption coefficient (α) of a direct band gap semiconductor, are related through the equation as follows αhν = C1(hν-Eg) where α is the linear absorption coefficient of the material, hν is the photon energy and C1 is a proportionality constant. When the material scatters in perfectly diffuse manner (or when it is illuminated at 601 incidence), the K–M absorption coefficient K becomes equal to 2α (K=2α). In this situation, considering the K–M scattering coefficient S as constant with respect to wavelength, and using the remission function we can obtain the expression: [F(R)hν]2 = C2(hν-Eg).

Therefore, by obtaining F(R) and plotting the [F (R) hν]^2 against hν, the band gap Eg of a powder sample can be extracted[113].

Diffuse reflectance spectroscopy (DRS) of (nanoscaled) powders is a frequently used and powerful instrument in material sciences and industry. An input light beam's scattered intensity

is scanned over the sample as a function of wavelength, and the resulting data set is analyzed in terms of macroscopic optical properties such as total reflectivity.

Furthermore, DRS can detect particle absorption characteristics even at sub-micron length scales. Absolute values of the absorption coefficient, as well as dispersive qualities, are crucial for a variety of materials with strong commercial potentials, such as pigments or phosphors. Absorption qualities influence the macroscopic optical properties of dielectric powders, but they also influence the losses of internally emitted light. As a result, DRS is routinely utilised in applications that fall short of its capabilities, and it is mostly used to determine macroscopic optical properties.

This method offers various advantages, including

1) high-quality reflectance spectra,

2) good consistency in calculating absorption features,

3) easy identification of signal artifacts, allowing for further reduction.

4.2 Ultraviolet-Visible Spectrophotometer

UV spectroscopy is a form of absorption spectroscopy in which molecules absorb light in the ultraviolet range (200–400 nm). The excitation of electrons from the ground state to higher energy states occurs as a consequence of the absorption of UV radiation. Since the ground state and higher energy states have different energies, the energy of the UV light that is absorbed is equal to that difference (E = h).

Two laws govern the absorption of light by a medium, known as Lambert's law and Beer's law. Lambert's law predicts the absorbance is directly proportional to the thickness/path length of the medium. Beer's law explains the effect of the concentration of colored components in a solution on light transmission or absorption. By combining these two laws, we get lambert Beier's law which is as follows:

$$\log (I_0/I_t) = A = \alpha cd$$

Where, A denotes absorbance, α denotes molar absorptivity, c is concentration and d is path length. According to Lambert-Beer's law, the amount of light absorption increases with the number of molecules that can absorb light of a particular wavelength. That is the fundamental idea behind UV spectroscopy.An equipment called a spectrophotometer evaluates a sample's

transmittance or absorbance about the wavelength of electromagnetic light. The main components of a spectrophotometer are:

1. Source
2. Monochromator
3. Sample container
4. Detectors

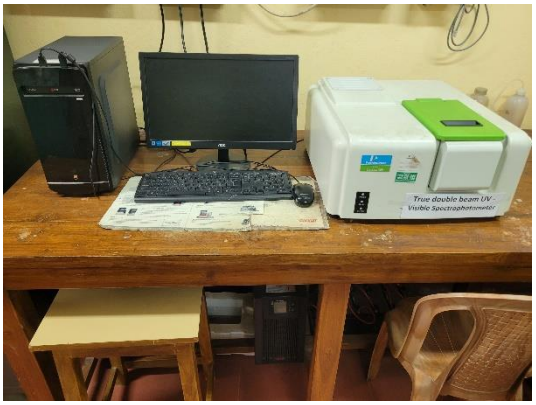


Figure 4: UV-Vis Spectrophotometer (Perkin Elmer UV-Vis Lambda 365)

4.3 Dynamic Light Scattering and Zeta-Potential Measurement

Particle Size and zeta potential of BNC samples were measured using the Malvern Zetasizer Nano-ZS instrument. BNC suspensions (0.1 wt. %) was equilibrated at room temperature for 1 hour and DLS was employed at 173° scattering angle in a temperature regulated cell at 25°C to obtain effective hydrodynamic diameters and size distributions. The hydrodynamic diameter was calculated using Stokes-Einstein equation while sample size distribution was obtained employing inverse Laplace transform. The zeta potential of the same samples was obtained using the same instrument but a sample cell holder equipped with electrode. The electrophoretic mobility of the samples was measured under an external electric field and the Smoluchowski equation was employed for zeta potential measurement of the samples. The DLS and Zeta potential values are an average of min 10 readings.

4.3.1 Dynamic Light Scattering (DLS)

DLS measures Brownian motion and relates this to the size of the particles. Brownian motion is the random movement of particles due to the bombardment by the solvent molecules that surround them.

Stokes-Einstein equation:

$$d(H) = \frac{kT}{3\pi\eta D}$$

d(H)= hydrodynamic diameter

D = translational diffusion coefficient (The velocity of the Brownian motion is defined by a property known as the translational diffusion coefficient, usually given the symbol, D)

k= Boltzmann's constant

T= absolute temperature

n= viscosity

The hydrodynamic diameter of a non-spherical particle is the diameter of a sphere that has the same translational diffusion speed as the particle.



Figure 5: DLS Zeta-potential instrument (Malvern Zetasizer)

4.3.2 Zeta potential

Zeta potential is a physical property which is exhibited by any particle in suspension, macromolecule, or material surface. The potential at the boundary (surface of hydrodynamic

shear) is the zeta potential. Zeta potential versus pH curve will be positive at low pH and lower or negative at high pH. The Zeta potential of the samples was calculated using the Smoluchowski equation.

Smoluchowski equation:

$$\zeta = u_{elf} \frac{\eta}{\varepsilon_r}$$

where, u_{elf} = electrophorectic mobility, ζ = viscosity of the medium, ε_r = relative permittivity.

4.4 Fourier Transform Infrared (FTIR) Spectroscopy

FTIR spectroscopy is a valuable tool for studying the vibrational properties of synthesized materials. The band positions and absorption peaks of thin films are influenced not only by their chemical composition and structure but also by their morphology. The preferred technique for infrared spectroscopy is Fourier Transform InfraRed (FT-IR). This method involves passing IR radiation through a sample, where the sample absorbs some of the radiation and transmits the rest. The resulting spectrum shows the molecular absorption and transmission of the sample, creating a molecular fingerprint. No two unique molecular structures produce the same infrared spectrum, making infrared spectroscopy versatile for various applications. FTIR can determine the quality or consistency of a sample. It can determine the number of components in a mixture and identify the unknown materials.

For over seventy years, infrared spectroscopy has been a fundamental technique in the laboratory for materials analysis. An infrared spectrum serves as a fingerprint for a sample, with absorption peaks corresponding to the frequencies of vibrations between the bonds of the material's atoms. Since each material consists of a unique set of atoms, no two compounds have identical infrared spectra. Consequently, infrared spectroscopy can be used to positively identify (qualitatively analyze) any type of material. Additionally, the size of the peaks in the spectrum indicates the amount of material present, making infrared spectroscopy an excellent tool for quantitative analysis, especially with the aid of modern software algorithms.

The standard instrumental procedure for infrared spectroscopy involves several steps. First, a glowing black-body source emits infrared energy. This beam passes through an aperture that regulates how much energy is delivered to the sample and, ultimately, to the detector. Next, the beam enters the interferometer, which performs "spectral encoding" and outputs the interferogram signal. The beam then enters the sample compartment, where it is either transmitted through or reflected off the surface of the sample, absorbing specific frequencies of energy unique to the sample. Finally, the beam reaches the detector, which is designed to measure the interferogram signal. The measured signal is then digitized and sent to a computer, where it undergoes Fourier transformation. The user is presented with the final infrared spectrum for interpretation and any further manipulation.



Figure 6: FTIR (Jasco FT/IR-4700)

5 Results & Discussion

5.1 Photocatalytic performance of prepared MoS_2 samples in dye degradation

Photocatalytic activity of the prepared materials under solar light has been discussed in this section. The effects of various parameters on photocatalytic performance of the prepared MoS_2 materials are also discussed in details.

5.1.1 Effect of synthesis parameters and additional chemicals used on the degradation performance of synthesized MoS_2

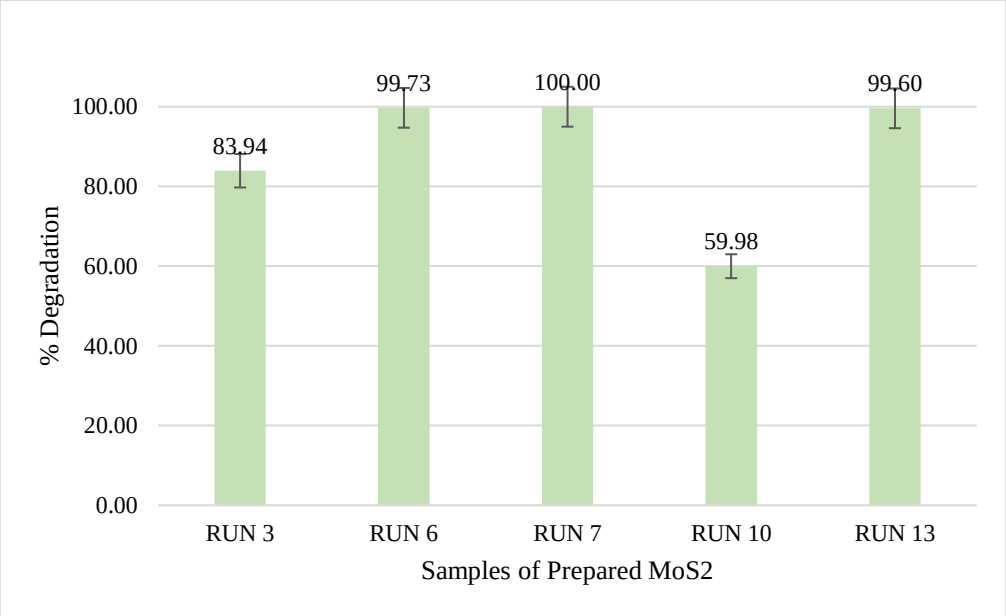
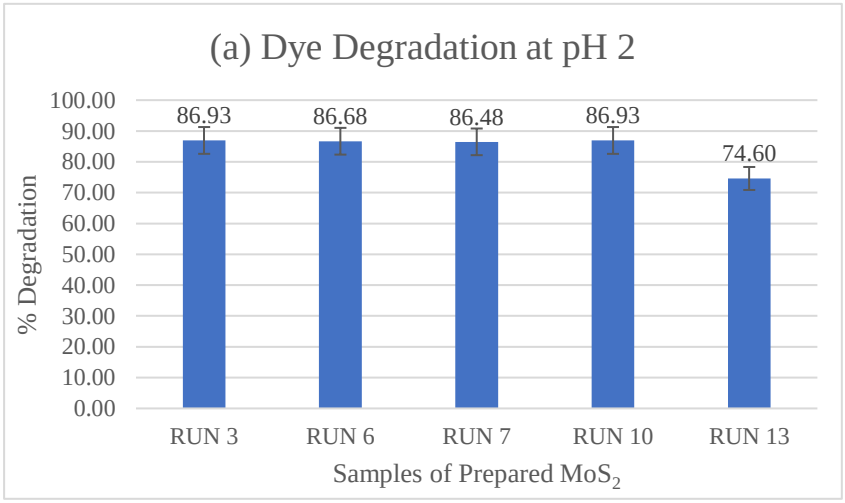


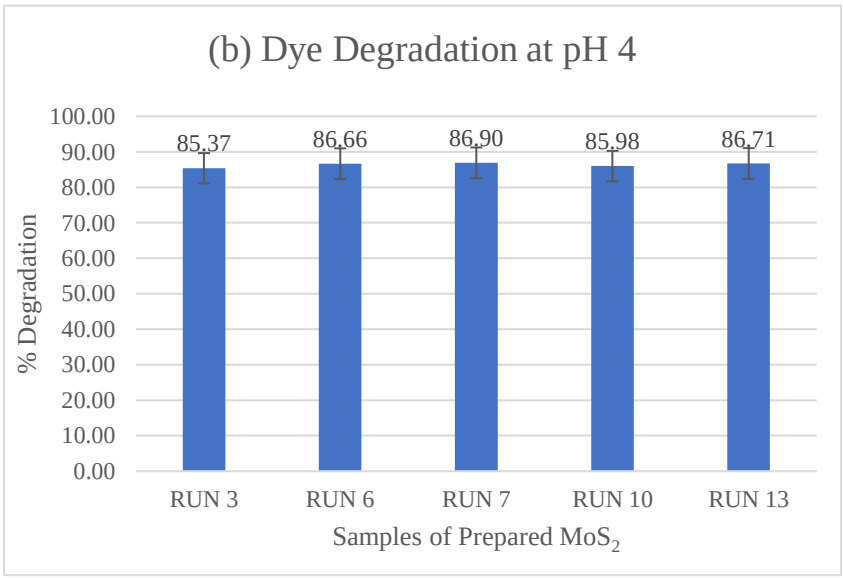
Figure 7: Effect of synthesis parameters and additional chemicals used on the degradation performance of synthesized MoS_2 towards 50ppm MG under sunlight

The five samples selected are on the basis of the yield of the final product, resulting from the various combinations of operating conditions, precursors, and added chemicals as shown in Table 4, considering the economic aspect, a reduced yield will not be feasible as a viable avenue for dye degradation. In the samples selected, run 6, 7 & 13, show the highest degradation of almost 100% for 50ppm MG solution under direct sunlight for 2 hours. Sample from Run 7 shows complete removal of dye, a 1: 2 molar ratio of Sodium Molybdate & Thiourea**,** and an excess amount of HCL, both may be considered as a factor for such degradation capability. The same molar ratio has been used in all other cases, however, the overall concentration of reactants provided in the hydrothermal reactor initially is the least in the case of run 7. This lower concentration during hydrothermal synthesis may be a reason for its superior

performance as a catalyst photocatalyst for dye degradation. Lower concentration of the reactants also leads to an excess of HCL which may have induced better photocatalytic attributes to the sample being synthesized during the hydrothermal treatment. Although Samples prepared in runs 6 and 13 show very high degradation capability, trace amounts of dye left untreated may have serious implications on the health of organisms, so their performance has to be improved in order to make them viable.

5.1.2 Effect of varying pH on the degradation performance of synthesized MoS_2





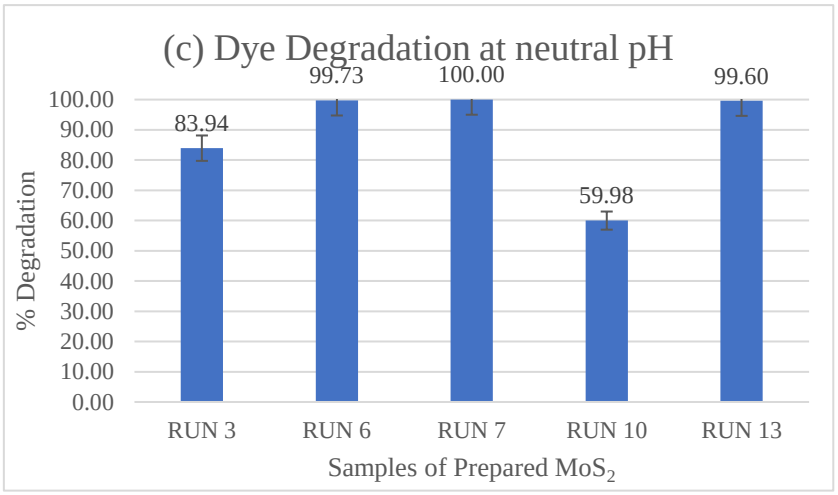


Figure 8: Degradation of malachite green dye at, (a) pH 2, (b) pH 4 and (c) neutral pH

The data in Figure 7 indicate that at pH2 and pH4 every sample degrades the dye to at most 86 percent in 2 hours. Only under the conditions of neutral pH, samples synthesized in RUN 7 is able to completely degrade the dye in 2 hours, this slight loss of degradation capacity in acidic conditions may be due to the cationic nature of malachite green, which in conjunction with H^+ ions present becomes more resistant to degradation against electron-hole pairs generated during photocatalysis. The excess H^+ ion concentration may also hinder mobility of the generated electron-hole pairs by recombination, leading to the generation of hydrogen gas, while a small fraction of dye remains unaffected. Analysis of dye degradation performance in varying conditions of basic medium has not been provided, as, OH• radicals in the basic medium interact immediately with the cationic dye and rupture the double bonds almost instantaneously, and further degradation of the dye by photocatalysis is no longer feasible for analysis. This may be overcome by the use of anionic or neutral dyes.

5.1.3 Effect of catalyst loading on the degradation performance of synthesized MoS_2

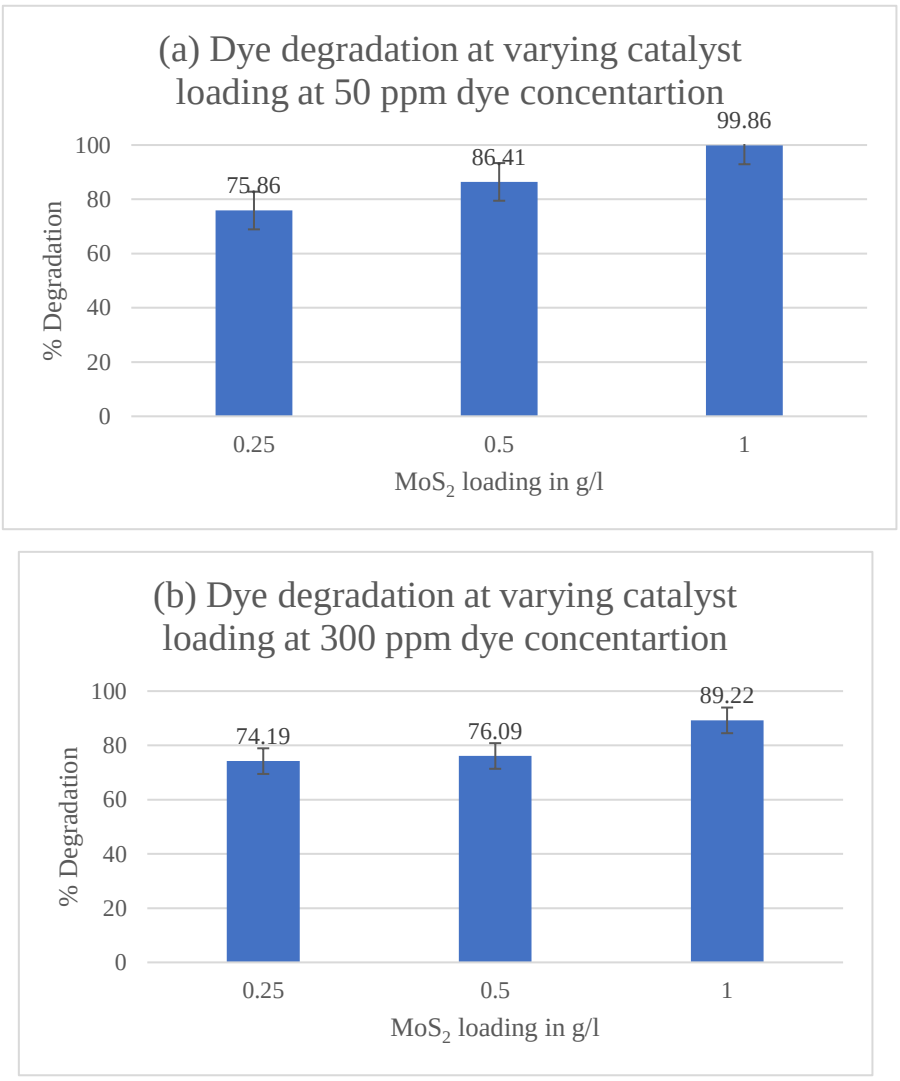


Figure 9: Dye degradation at varying catalyst loading at, (a) 50 ppm, and (b) 300 ppm malachite green concentration

Under neutral conditions, the effect of catalyst loading on dye degradation was investigated. Increased loading of MoS_2 samples from Run 7 led to better degradation performance. The dye degradation capability follows a nearly linear trend with increasing loading. The degradation at 50 ppm is almost 100%, with a slight amount of dye remaining, which may be the result of reduced sunlight availability during the end of the experiment. The degradation observed for 300 ppm dye concentration is not fully complete, as the increased concentration of dye, may hinder sunlight from reaching the catalyst surface, and a reduction of the intensity due to

scattering by the dye particles. So, considering the discussion in section 5.1.1, MoS_2 prepared in Run 7 may be considered the best photocatalyst candidate, a neutral pH may be considered as the optimal condition for malachite green degradation as per section 5.1.2, and a loading of 1g/L may be considered as the best catalyst loading.

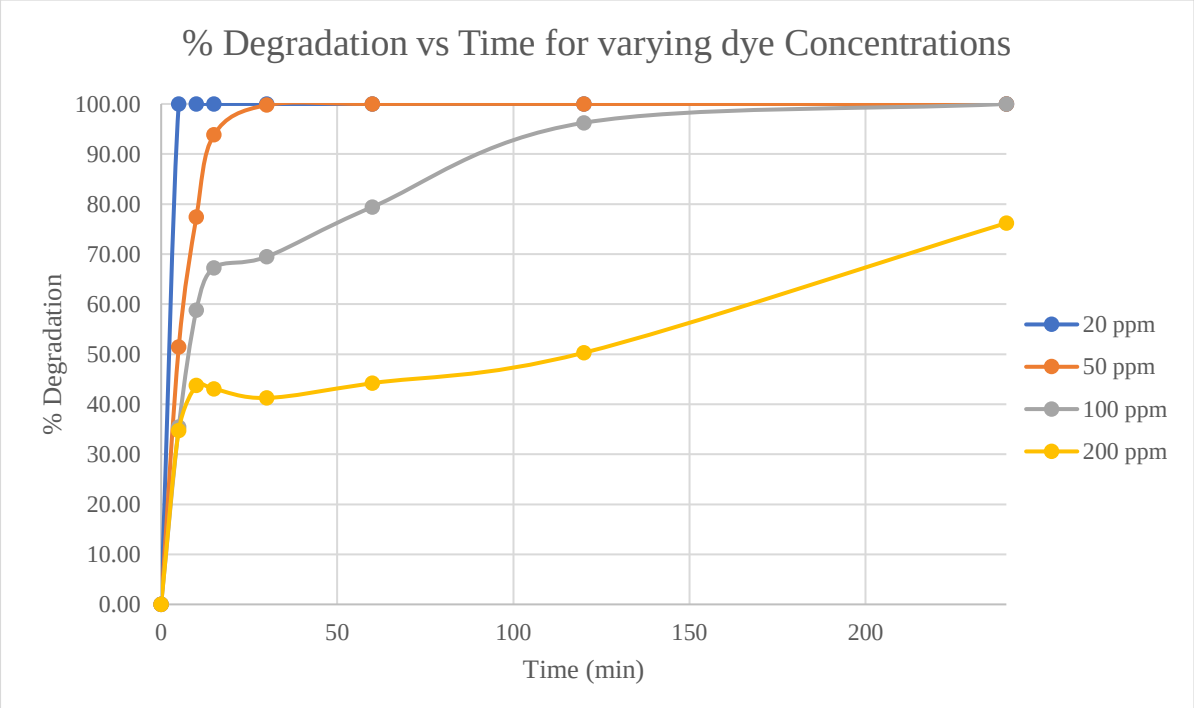


Figure 10: Effect of dye concentration and contact time on the dye degradation performance of synthesized MoS_2

5.1.4 Effect of dye concentration on the dye degradation performance of synthesized MoS_2

MoS_2 synthesized in Run 7, shows up to 100% dye degradation potential for malachite green dye concentration of up to 100 ppm, within four hours for a loading of 1g/L and in neutral pH. The degradation is fast, with complete degradation of the dye being achieved within 30 minutes of exposure to sunlight for concentrations up to 50 ppm, while the dye concentration of 100 ppm requires about 200 minutes. This may be due to the increased difficulty of sunlight in reaching the catalyst surface due to interference from dye particles at higher concentrations as discussed in section 5.1.3. This same phenomenon may be responsible for incomplete

degradation in the case of the dye concentration of 200 ppm. The experiment has not been carried out further, due to the loss of available sunlight during the particular day of the experiment.

5.1.5 Kinetics of Photocatalytic dye degradation by synthesized MoS_2

The heterogeneous reaction includes two consecutive steps. Firstly, the reactants are adsorbed on the surface of the photocatalysts and secondly, the photocatalytic reaction commences. In general, the adsorption rate is slower than the photocatalytic reaction rate. So, the overall photocatalytic reaction rate is mainly dominated by the adsorption rate. Furthermore, the adsorption rate can be equivalently expressed using the coverage ratio of the adsorbed reactants on the surface of the photocatalysts. So, the photocatalytic reaction rate r can be expressed as the following equation, which is widely known as the original Langmuir-Hinshelwood model.

$$r = -\frac{dC}{dt} = k_p\theta$$

where c is the concentration of the reactant, t is the photocatalytic reaction time, θ is the coverage ratio of pollutants on the MoS_2 surface, k_p is the photoreaction coefficient. According to Langmuir's adsorption theory, the coverage ratio is related to adsorption capacity and the concentration of the reactant. K_L was defined as an adsorption equilibrium constant to measure the adsorption capacity of MoS_2 and coverage ratio θ may be expressed as: $\theta = \frac{K_L C}{1+K_L C}$

Therefore, the photoreaction coefficient r may be expressed as $r = k_p \frac{K_L C}{1+K_L C}$ which may further be approximated as: $r = -\frac{dC}{dt} = k_{ap} C$. The solution to this first-order differential equation with boundary conditions $C=C_0$ at $t= 0$ yields:

$$\ln (C_0/C) = k_{ap} t$$

Hence a plot of $\ln (C_0/C)$ versus t should yield a straight line with slope k_{ap}.

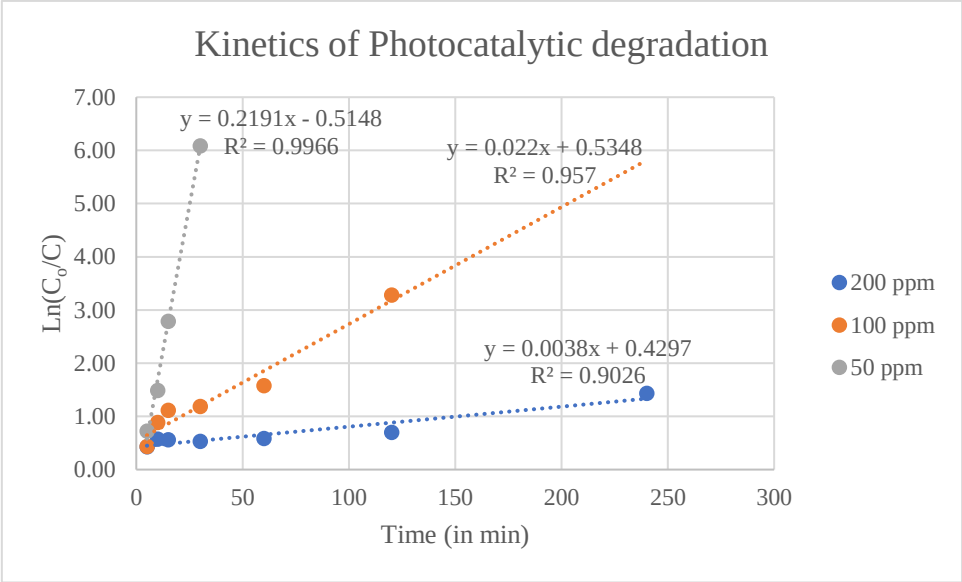


Figure 11: Kinetics of Photocatalytic dye degradation by synthesized MoS_2

Three sets of data were considered for kinetic analysis, namely dye concentrations of 50 ppm, 100 ppm & 200 ppm, with a catalyst loading of 1 g/L at neutral pH. A dye concentration of 20 ppm was not considered due to the lack of meaningful data points beyond the first few minutes, as degradation of dye was almost instantaneous. This instantaneous degradation may be attributed to the large availability of catalyst surface for the dye particles due to low θ, on account of less hindrance due to the low concentration of dye particles. A lower dye concentration yields a better fit with the Langmuir-Hinshelwood model, this may be due to the reduced interactions among the dye particles at lower concentration, and also the greater availability of catalyst surface area available. The increase in dye concentration leads to subtle deviation from the data predicted by the model, this may be due to, a) hindrance by dye particles among themselves, preventing a direct path towards the catalyst surface, b) less available catalyst surface area, & c) as discussed in section 5.1.4, increased concentration of dye particles hinders the available sunlight from reaching the catalyst surface. The degradation process may not be the rate-determining step, as observed from the agreement with the Langmuir-Hinshelwood, however, the lack of available sunlight on the surface of the catalyst may have a significant effect on the dye degradation capability of MoS_2. The improved degradation observed in case of lower dye concentration is also indicated by the slope, the k_{ap} value of the curve. The value in case of 50 ppm dye concentration is 0.291, which is nearly 10 times greater than the k_{ap} value (0.022) for 100 ppm dye concentration. The k_{ap} value observed for the 200

ppm dye concentration is 0.038 is almost five times lower than at 100 ppm dye concentration. The correlation between the dye concentration and the effectiveness of the photocatalyst may be considered to be more predominant at higher concentrations of dyes and the conditions discussed earlier regarding deviations from the predicted model may be the reason for the same.

5.2 Characterization of prepared MoS_2 samples

5.2.1 UV-Vis Diffuse Reflectance Spectroscopy

Table 5: Band gap of different MoS_2 samples

Sample Name	Band gap (eV)
Run 3	3.61
Run 7	3.6
Run 13	3.76

These values indicate that the band gaps of the samples slightly vary, with Run 13 exhibiting the widest band gap among them.

DRS combined with Tauc's plot analysis provided valuable insights into the optical properties of MoS_2 samples. Generally, narrower band gaps (as observed in Run 7 and Run 3) are associated with enhanced visible-light absorption, which can promote photocatalytic activity under solar radiation. Run 7, with a band gap of 3.6 eV, appears to be well-suited for absorbing solar photons and generating electron-hole pairs efficiently, thereby facilitating the degradation of malachite green dye. The observed band gap variations among the samples directly influenced their photocatalytic performance, with Run 7 demonstrating superior efficiency in the degradation of malachite green dye under solar radiation as seen in section 5.1.1. These findings underscore the significance of band gap engineering for optimizing the photocatalytic capabilities of MoS_2 and similar semiconductor materials in environmental remediation applications. Samples from Run 13 followed closely as the second-best performer in terms of dye degradation efficiency, however, it should have inferior performance as compared to samples from Run 3, this may have been due to the presence of ascorbic acid during synthesis which enables easier promotion of electron-hole pairs due to its highly branched structure.

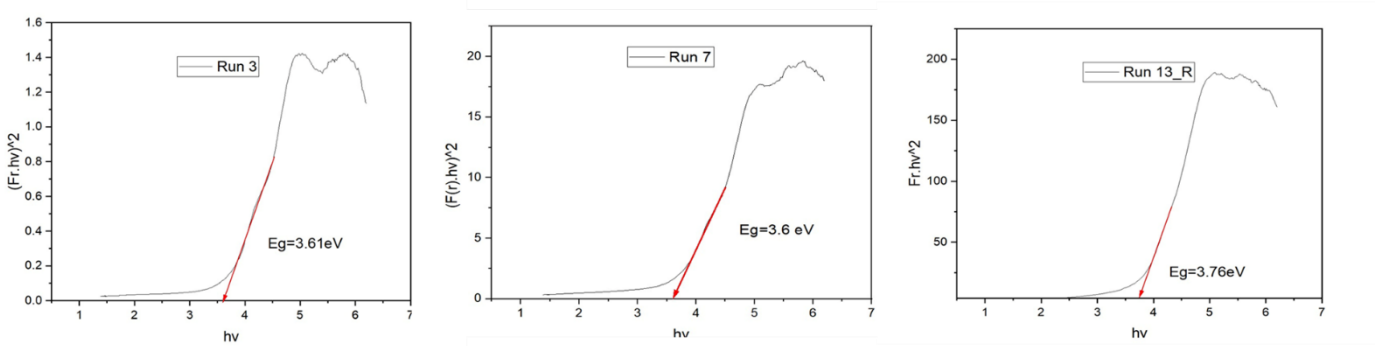


Figure 12: Tauc's plot for synthesized MoS_2 samples

5.2.2 Particle size & Zeta potential analysis

5.2.2.1 Particle size analysis by DLS

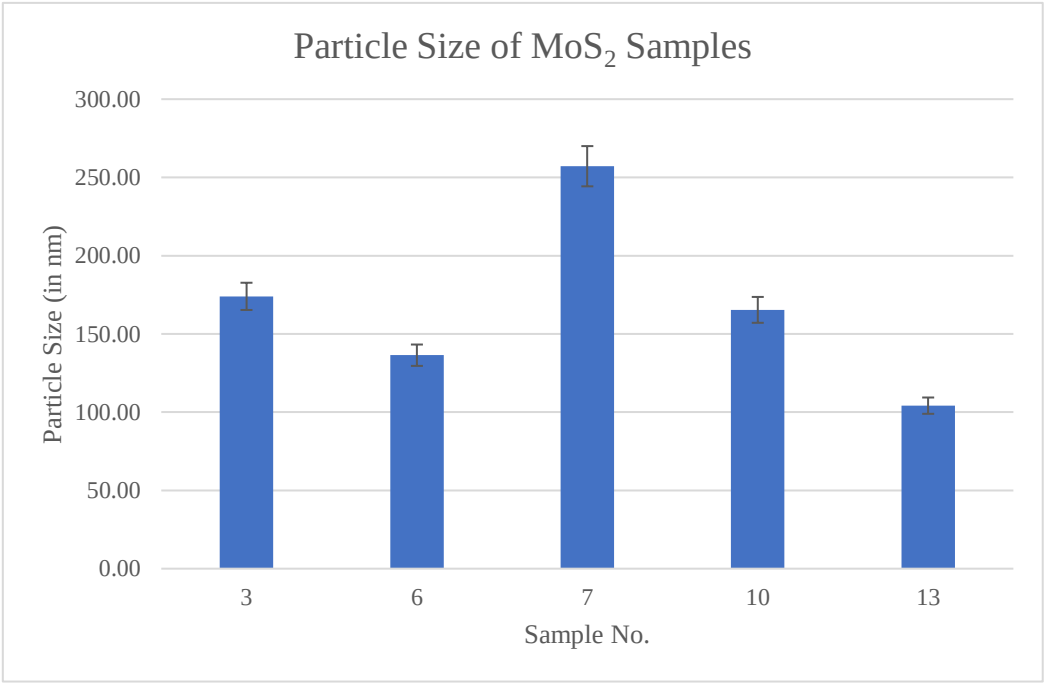


Figure 13: Particle size analysis of MoS_2 samples selected for dye degradation experiments

The DLS measurements provide critical insights into the size distribution of the synthesized MoS_2 nanoparticles. The hydrodynamic diameters recorded from the five runs exhibit variability, with values ranging from 104.17 nm to 257.17 nm.

Run 3 (174.00 nm): The hydrodynamic diameter of 174.00 nm suggests that the synthesized nanoparticles are relatively uniform in size, with a moderate distribution likely influenced by the synthesis conditions.

Run 6 (136.40 nm): The observed diameter of 136.40 nm is smaller compared to Run 3, indicating a tighter control of particle size in this run. This could be due to variations in synthesis parameters such as temperature, reaction time, or precursor concentration.

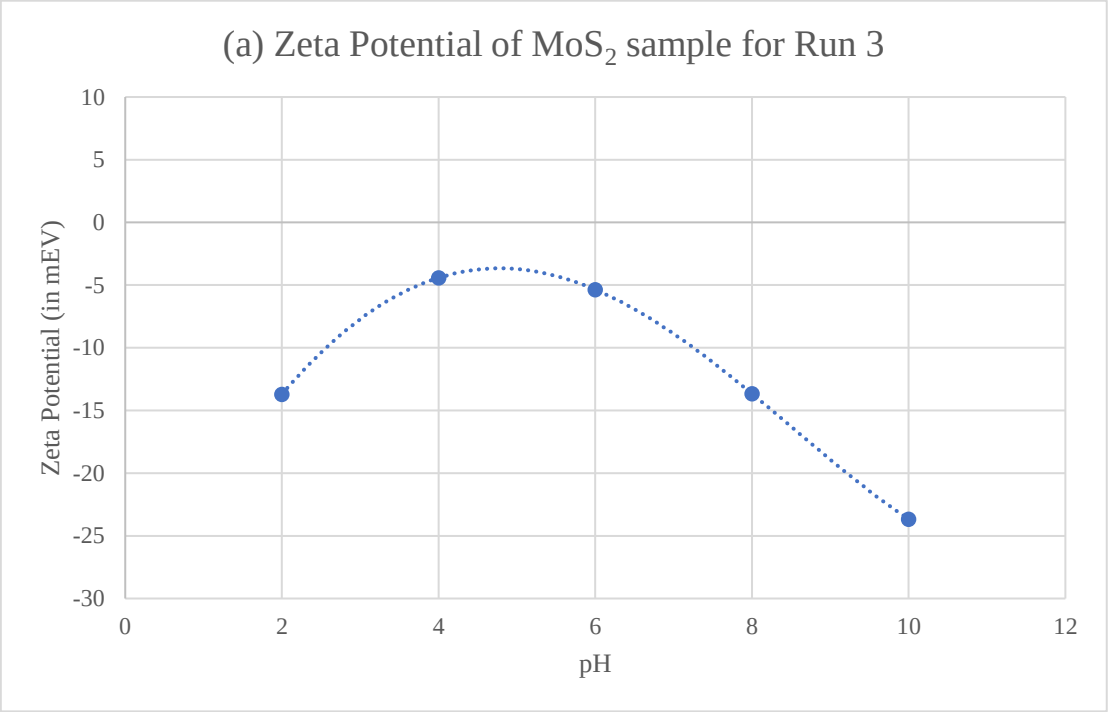
Run 7 (257.17 nm): This run shows a significantly larger diameter, suggesting possible agglomeration or the presence of larger particles. Such deviations can be attributed to inconsistencies in the synthesis process or variations in the precursor quality.

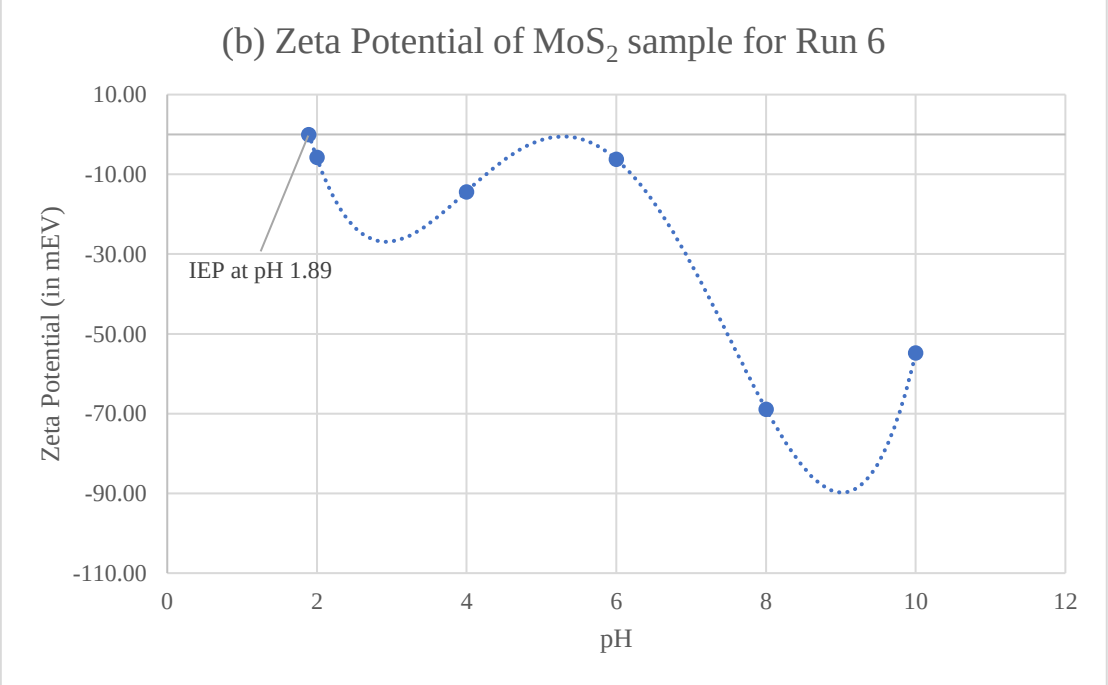
Run 10 (165.37 nm): Similar to Run 3, Run 10 shows a hydrodynamic diameter of 165.37 nm. The consistency between these runs suggests reproducibility in the synthesis method under similar conditions.

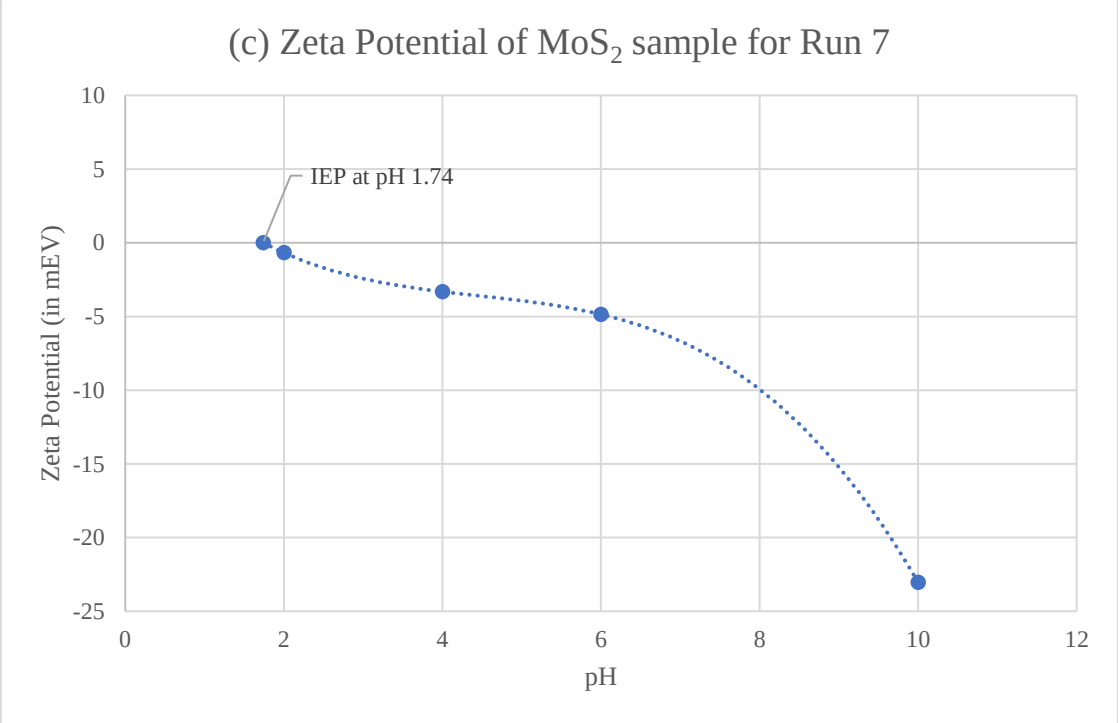
Run 13 (104.17 nm): The smallest diameter recorded is 104.17 nm, indicating a potentially more effective control over nanoparticle size. This could result from optimized synthesis parameters or the presence of a stabilizing agent during the synthesis process.

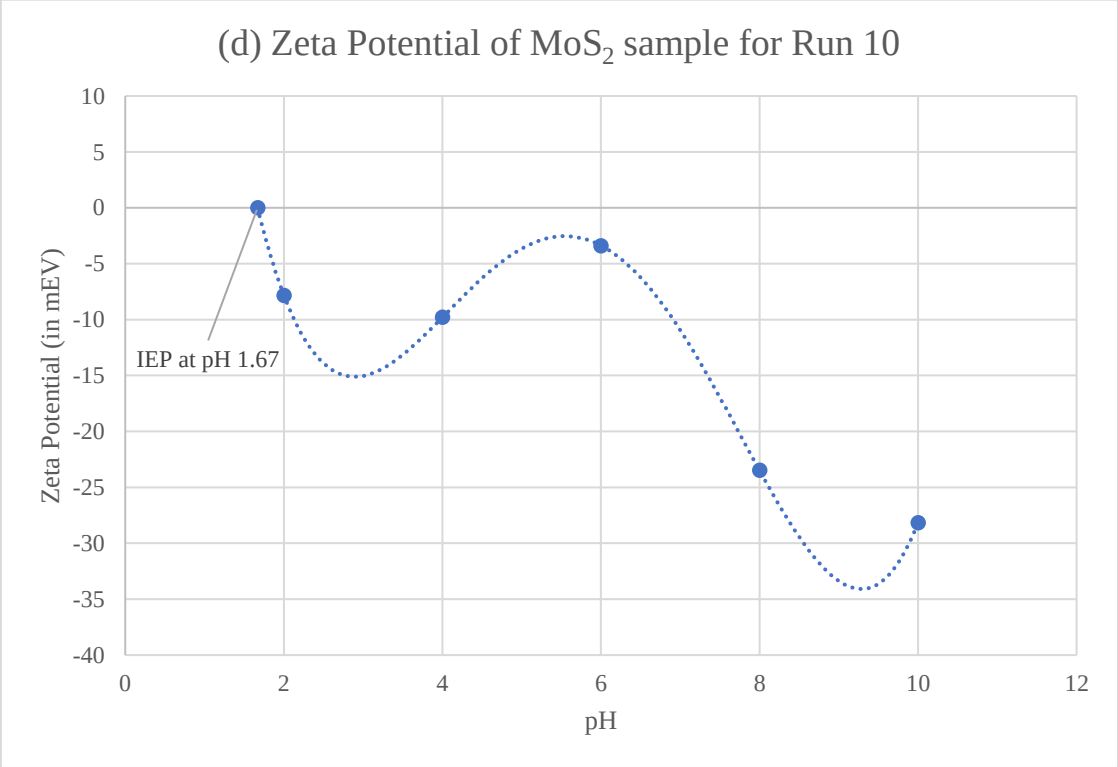
The variability in hydrodynamic diameter across different runs has significant implications for the application of MoS_2 nanoparticles. Smaller, uniformly sized particles, as seen in Run 13, are advantageous for applications requiring high surface areas and uniform reactivity, such as catalysis or electronic devices, and larger particles or aggregates, as seen in Run 7, maybe less desirable for such applications but could be beneficial in other contexts where bulk material properties are prioritized. As discussed in Figure 6, during dye degradation Run 7 performs better than Run 13, which may be due to the formation of highly interlinked and porous structured MoS_2 (flower-shaped) during synthesis due to an excess of H^+ ions from HCl. The degradation performance of samples from Run 3 & 10 may be due to the reduced surface area available for the dyes to be adsorbed on to.

5.2.2.2 Zeta-Potential Analysis






(c) Zeta Potential of MoS2 sample for Run 7
IEP at pH 1.74
Zeta Potential (in mEV)
pH
10
5
0
-5
-10
-15
-20
-25
0
2
4
6
8
10
12


(d) Zeta Potential of MoS2 sample for Run 10
IEP at pH 1.67
Zeta Potential (in mEV)
pH
10
5
0
-5
-10
-15
-20
-25
-30
-35
-40
0
2
4
6
8
10
12

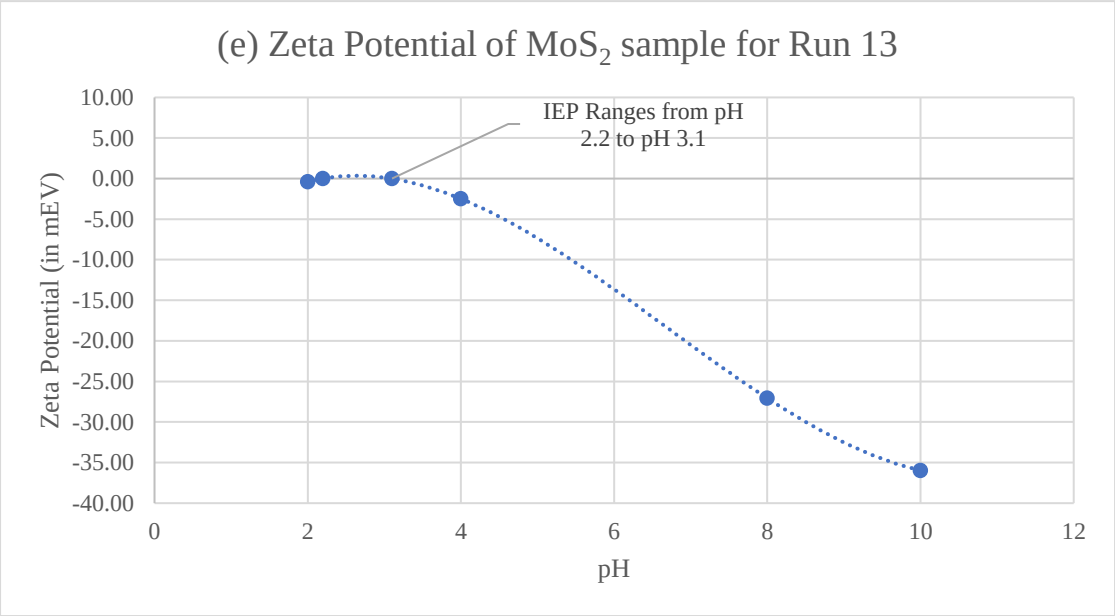


Figure 14: Zeta potential and Isoelectric points of investigated MoS_2 samples

Table 5: pH values at which the samples in suspension display their isoelectric point

Sample	Iso electric point (pH)
RUN 3	No IEP
RUN 6	1.89
RUN 7	1.74
RUN 10	1.67
RUN 13	2.2 to 3.1

RUN 3 demonstrated no suspension stability over the pH range examined, with no isoelectric point (IEP) within the investigated pH range. RUN 6's IEP is located at pH 1.89, and the surface charge over the investigated range show that a stable suspension is only formed by the catalysts at beyond pH 6. RUN 7 also had its IEP at an acidic 1.74, suggesting a similar but marginally different behavior about charge neutrality and particle suspension stability. At pH 1.67, RUN 10 had an even lower IEP, indicating a change in the point of zero charge's circumstances toward acidity. Significantly, RUN 13's IEP range was vast, ranging from pH 2.2 to 3.1. This might mean that a variety of components with different charge characteristics are present due

to the utilization of a branched acid during synthesis, or that the pH stability range is larger (most likely from precursor). These differences in IEPs among the samples highlight their diverse surface charge characteristics and potential implications for their stability and interactions in different pH environments. Also, at neutral pH, all samples show a negative surface charge, which facilitate them as good adsorbents for cationic dyes. The reduction in the electronegativity at higher pH may be considered as the reason for reduced dye degradation performance at acidic pH conditions as seen in Figure 7, in section 5.1.2.

5.2.3 FTIR Analysis

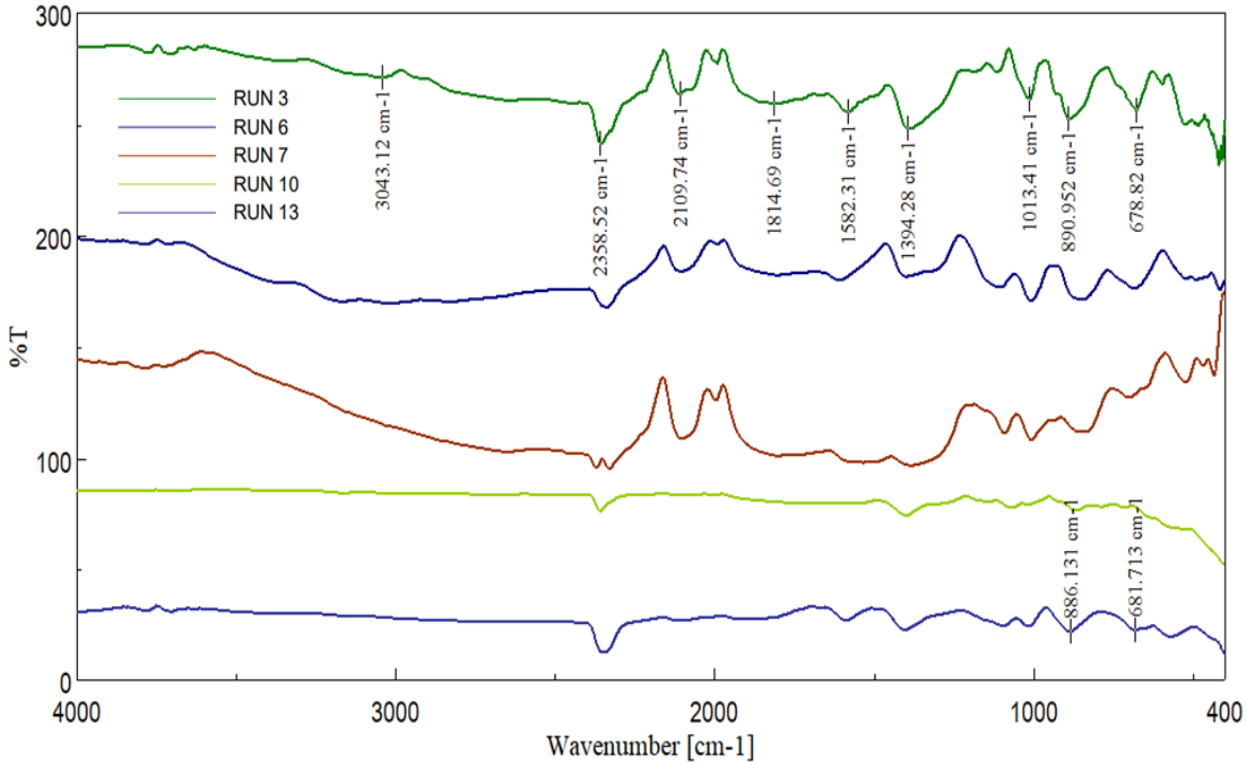


Figure 15: FTIR spectra of MoS_2 samples under investigation

Figure 10, depicts the FTIR spectrum for the samples labelled as RUN 3, RUN 6, RUN 7, RUN 10, and RUN 13 in the range of 400 cm^{-1} to 4000 cm^{-1}. The broad band from 3000 cm^{-1} to 3800 cm^{-1} corresponds to the stretching (υ) vibrations of the hydroxyl O-H groups, which is absent from Run 10 and Run 13, which may be due to the use of Sulphuric acid, a dehydrating acid during synthesis. The band at 2358.52 cm^{-1} is associated with the asymmetric stretching vibration of CO_2 molecules. Its presence suggests the potential for adsorption of atmospheric CO_2 on the surface of the samples. The four bands at 2109.74 cm^{-1},1814.69 cm^{-1},1582.31 cm^{-1} and 1394.28 cm^{-1} is associated with C≡C, C=O, C=C, and CH_x groups implying that some organic material is present via precursors or through atmospheric contaminants. The band

between 850 cm^{-1} to 950 cm^{-1} corresponds to the stretching (υ) vibrations of the S-S bond. The band between 650 cm^{-1} to 750 cm^{-1} corresponds to the asymmetric wagging vibrations of the Mo-S bond. The FTIR spectra indicate the successful synthesis of MoS_2, as evidenced by the presence of characteristic Mo-O and Mo-S stretching vibrations. The peaks at 678.82 cm^{-1}, 681.71 cm^{-1}, and 890.95 cm^{-1} confirm the formation of Mo-S bonds, which are critical for the structural integrity and degradation capability of the synthesized MoS_2. The absence of clear Mo-S bonds in samples from Run 10, is mirrored in its weaker degradation capability as compared to others as seen in section 5.1.1. Although samples from Run 3 have clearly defined Mo-S characteristics, the degradation performance observed is not comparable to that of Run 7, which may result from a reduced synthesis temperature leading to MoS_2 structures of lower surface area, with reduced capability towards dye degradation. The spectra also reveal the presence of various organic and inorganic impurities, as indicated by the peaks at 2358.52 cm^{-1}, 2109.74 cm^{-1}, 1814.69 cm^{-1}, 1582.31 cm^{-1}, 1394.28 cm^{-1}, and 1013.41 cm^{-1}. These impurities could stem from the synthesis process, atmospheric exposure, or contamination during sample preparation. The peak at 2358.52 cm^{-1} suggests CO_2 adsorption, which is common when samples are exposed to air. The presence of carbon-based materials, indicated by the peaks at 2109.74 cm^{-1} and 1582.31 cm^{-1}, may result from organic residues left over from the synthesis or handling processes, where a Teflon seat is involved which has undergone considerable decay during hydrothermal synthesis. The peak at 1013.41 cm^{-1} suggests silicate contamination, possibly from the equipment or environment.

6 Conclusion

MoS_2-based photocatalysts have been synthesized under various conditions as depicted in Table 4 of section 3.3. The prepared samples have been initially classified based on the yield and the synthesized material with the highest yield among varying synthesis parameters has been selected, experiments of photocatalytic degradation of malachite green dye have been carried out using the selected samples. These experiments have yielded various insights. Characterizations carried out on the same samples have shed some further light on the underlying reasons for the variation in the dye degradation capability of the synthesized samples. This study successfully synthesized MoS_2 samples through hydrothermal methods and evaluated their photocatalytic performance in dye degradation. The key findings of this research may be summarized as follows:

1. **Synthesis Parameters**: The molar ratios and chemical concentrations used during synthesis had a major effect on the MoS_2 samples' photocatalytic efficiency. Under sunlight, samples synthesized in Run 7, in particular, have shown the best degradation efficiency of malachite green dye under neutral pH conditions. Samples in all the runs have been prepared with a 1:2 molar ratio of sodium molybdate and thiourea, however, the addition of HCL may be considered as a primary reason for the better performance of Run 7 samples as compared to those in Run 10 & 13. Among samples from Run 3,6 & 7, the higher temperature of synthesis, 200^oC in Run 7 as compared to 180^oC in Run 3 may have led to the formation of photocatalysts with improved surface properties. Comparing Run 6 & 7, the abundance of HCL, leads to an increase in H^+ ions which may have facilitated better interlinking of Mo and S atoms after the cleavage of the precursors leading to the formation of flower-shaped MoS_2 nanoparticles at the higher temperature during the hydrothermal method, which may have been the reason for improved photocatalytic characteristics.
2. **Effect of pH and catalyst loading**: The degradation efficiency was not constant across all pH values. As observed Figure 7 in section 5.1.2, the dye degradation performance of samples from Run 7 was the best in neutral pH, totally breaking down the dye after two hours. The degradation efficiency was somewhat reduced and mostly similar for all samples in acidic circumstances (pH 2 and pH 4), most likely as a result of cationic dye molecules interacting with excess H+ ions to impede the photocatalytic process. Figure 8 in section 5.1.3 shows that the degradation efficiency was improved up to a particular concentration by increasing the catalyst loading. 1g/L was assumed as an

ideal loading for efficient photocatalysis as there was complete degradation observed for 50ppm dye concentration at this limit. As excess concentration of dye hinders both the adsorption of dye particles on the catalyst surface, and also prevent the solar radiation from reaching the same, an excess loading may not necessarily improve degradation capability at a higher dye concentration. This may be further investigated as suitable modifications to the geometry of the reactor may help to overcome this problem.

3. **Characterizations** as discussed in section 5.2 have highlighted some interesting results, UV-Vis Diffuse Reflectance Spectroscopy, used to analyze the MoS_2 samples indicated a band gap in the visible region, this promotes photocatalytic activity in sunlight eliminating the need for specialized spectra-based reactors. The band gap of samples from Run 7 is 3.6 eV is lower among all investigated samples as seen in Figure 11, and is in agreement with the dye degradation performance. Particle size analysis in Figure 12 in section 5.2.2, indicates a higher particle size for Run 7, which will lead to a reduced specific surface area, however, this effect should reduce the dye degradation capability, but it may have been offset due to a more branched flower shaped geometry due to an excess of H^+ ions during synthesis conditions. Zeta potential analysis indicates that the synthesized catalysts form mostly unstable suspensions, however, the surface charge observed is negative, and this helps in the easier transfer of cationic dyes to the catalyst surface. FTIR spectra of the samples as seen in Figure 14, show the formation of Mo-S bonds and S-S bonds, characteristic of MoS_2 nanoparticles from well-defined peaks at 850 cm^{-1} to 950 cm^{-1} corresponding to the stretching (υ) vibrations of the S-S bond, between 650 cm^{-1} to 750 cm^{-1} corresponds to the asymmetric wagging vibrations of the Mo-S bonds. Peaks at at 678.82 cm^{-1}**,** 681.71 cm^{-1}**,** and 890.95 cm^{-1} indicate the structural integrity and degradation capability of synthesized MoS_2.
4. **Kinetic Analysis**: According to the kinetic investigations, photocatalytic activity improved with decreasing dye concentrations, and is consistent with the Langmuir-Hinshelwood model. Sunlight and the availability of catalyst surface area were important variables influencing the pace of deterioration.

The findings of this study contribute to the understanding of MoS_2 photocatalysts and provide a foundation for further research aimed at improving the efficiency and applicability of these materials in real-world environmental scenarios.

7 References

1. Newton, Marshall D., et al. "Electron transfer in chemistry." (2001).
2. ArnulfJager-Waldau, Solar Energy Materials and Solar Cells, Volume 95, Issue 6, June 2011, Pages 1509-1517
3. K. Aryal, B. N. Pantha, J. Li, J. Y. Lin, and H. X. Jiang, Applied Physics Letters 96, 052110 (2010)
4. Ludmila P. Oleksenko, Nelly P. Maksymovych, Evgeniy V. Sokovykh, Igor P. 28 Matushko, Andrii I. Buvailo, Norman Dollahon, Sensers and Actuators B 196 (2014) 298-305
5. A. Ohtomo, M. Kawasaki, T. Koida, K. Masubuchi, H. Koinuma, Y. Sakurai, Y. Yoshida, T. Yasuda, and Y. Segawa, Applied Physics Letters 72, 2466 (1998)
6. Ryu Abe, Kazuhiro Sayama, and Hideki Sugihara, J. Phys. Chem. B 2005, 109, 16052-16061
7. Nanostructures and Nanomaterials: Synthesis, Properties and Applications; Guozhong Cao.
8. https://www.nano.gov/nanotech-101/what/ definition.
9. Journal of Faculty of Engineering & Technology, 2007, 2008, pages, 1120.
10. Introduction to Nanoscience, Kai Nordlund 2005.
11. P. Motiarty, Rep. Prog. Phys. 64 (2001) 297.
12. Sinha, Tridib Kumar. "Morphology-dependent visible light photocatalysis." Nanostructured Materials for Visible Light Photocatalysis. Elsevier, 2022. 375-412.
13. Kuo-Feng Lin, Hsin-Ming Cheng, Hsu-Cheng Hsu, Li-Jiaun Lin, Wen-Feng Hsieh, Chemical Physics Letters 409 (2005) 208-211
14. O. Vigil, F. Cruz, A. Morales-Acevedob, G. Contreras-Puente, Materials Chemistry and Physics 68 (2001) 249-252
15. G. Anil Kumar, M. V. Ramana Reddy, KattaNarasimha Reddy, Journal of Physics: Conference Series 365 (2012) 012031

16. H. Merzouk, A. Chelouche, S. Saoudi, D. Djouadi, A. Aksas, ApplPhys A (2012) 109: 841-844

17. B. SrinivasaRao, V. Rajagopal Reddy, B. Rajesh Kumar, T. SubbaRao, International Journal of Nanoscience, Vol. 11, No. 3 (2012) 1240006(5pages)

18. SoumenDhara, P. K Giri, Journal of Experimental Nanoscience, 8(2013) 3, 332-340. 29

19. C. Suryanarayana, Bull. Mater. Sci., 17 (1994) 307

20. G. A. Ozin and A. C. Arsenault, Nanochemistry, RSC Publishing,Cambridge,UK, 2005.

21. H. W. Kroto, J. R. Heath, S. C. O'Brien, R. F. Curl and R. E. Smalley, Nature, 1985, 318, 162–163.

22. S. Iijima, Nature, 1991, 354, 56–58.

23. K. S. Novoselov, A. K. Geim, S. V. Morozov, D. Jiang, Y. Zhang, S. V. Dubonos, I. V. Grigorieva and A. A. Firsov, Science, 2004, 306, 666–669.

24. Gomez-Navarro, M. B. C., J. Gomez-Herrero, and F. Zamora. "2D materials: To graphene and beyond." Nanoscale 3.1 (2011): 20.

25. Novoselov KS, Geim AK, Morozov SV, Jiang D, Zhang Y, Dubonos SV, et al.Electric field effect in atomically thin carbon films. Science 2004;306:666e9.

26. Allen MJ, Tung VC, Kaner RB. Honeycomb carbon: a review of graphene. Chem Rev 2010;110:132e45.

27. Soldano C, Mahmood A, Dujardin E. Production, properties and potential of graphene. Carbon 2010;48:2127e50.

28. Bae S, Kim H, Lee Y, Xu X, Park JS, Zhang Y, et al. Roll-to-roll production of 30-inch graphene films for transparent electrodes. Nat Nanotechnol 2010;5:574e8.

29. Yagub, M. T., Sen, T. K., Afroze, S., & Ang, H. M. (2014). Dye and its removal from aqueous solution by adsorption: a review. *Advances in Colloid and Interface Science*, 209, 172-184.

30. Forgacs, E., Cserháti, T., & Oros, G. (2004). Removal of synthetic dyes from wastewaters: a review. *Environment International*, 30(7), 953-971.

31. Chhowalla, M., Shin, H. S., Eda, G., Li, L. J., Loh, K. P., & Zhang, H. (2013). The chemistry of two-dimensional layered transition metal dichalcogenide nanosheets. *Nature Chemistry*, 5(4), 263-275.

32. Gao, Y., Xu, J., & Sun, Y. (2016). Adsorption of methylene blue onto functionalized MoS_2 nanosheets. *Materials Science and Engineering: B*, 205, 1-7.

33. Xu, Y., Hong, H., & Wang, J. (2013). MoS_2 nanosheets as a highly efficient adsorbent for the removal of dye pollutants. *Journal of Materials Chemistry A*, 1(23), 6737-6743.

34. Chen, Y., Wang, F., Peng, S., & Zhai, J. (2015). Photocatalytic degradation of dye pollutants on MoS_2/TiO_2 heterostructures. *Applied Surface Science*, 351, 391-396.

35. (35) Wang et al. (2012). MoS2 nanosheets: Preparation, properties, and applications. Materials Today, 15(10), 434-442.

36. (36) Zhang et al. (2019). MoS2: A promising material for electronic and energy applications. Materials Science and Engineering: R, 137, 1-23.

37. (37) Li et al. (2020). MoS2 for energy storage and conversion: A review. Journal of Power Sources, 451, 227-238.

38. (38) Mak et al. (2010). Atomically thin MoS2: A new direct-gap semiconductor. Physical Review Letters, 105(13), 136805.

39. (39) Wang et al. (2019). MoS2 as a catalyst for hydrogen evolution reaction: A review. Journal of Catalysis, 375, 1-15.

40. (40) Liu et al. (2019). Synthesis of MoS2 nanosheets: A review. Chemical Society Reviews, 48(3), 636-648.

41. (41) Zhang et al. (2019). Sol-gel processing of MoS2 nanosheets. Journal of Sol-Gel Science and Technology, 91(2), 242-252.

42. (42) Yang et al. (2020). MoS2 for biomedicine: A review. Biomaterials, 252, 120-135.

43. (43) Chen et al. (2019). MoS2 for environmental applications: A review. Environmental Science: Nano, 6(2), 341-355.

44. Yang, D., S. J. Sandoval, W. M. R. Divigalpitiya, J. C. Irwin, and R. F. Frindt. 1991. Structure of single-molecular-layer MoS2. Phys. Rev. B 43:12053–12056.

45. Late, D. J., B. Liu, H. S. S. R. Matte, V. P. Dravid, and C. N. R. Rao. 2012. Hysteresis in single-layer MoS2 field effect transistors. ACS Nano 6:5635–5641.

46. Ataca, C., M. Topsakal, E. Aktürk, and S. Ciraci. 2011. A comparative study of lattice dynamics of three-and two-dimensional MoS2. J. Phys. Chem. C 115:16354–16361.

47. Ataca, C., H. S¸ahin, and S. Ciraci. 2012. Stable, single-layer MX2 transition-metal oxides and dichalcogenides in a honeycomb-like structure. J. Phys. Chem. C 116:8983–8999.

48. Beal, A. R., J. C. Knights, and W. Y. Liang. 1972. Transmission spectra of some transition metal dichalcogenides. II. Group via: trigonal prismatic coordination. J. Phys. C: Solid State Phys. 5:3540. 31

49. Shirodkar, S. N., and U. V. Waghmare. 2014. Emergence of ferroelectricity at a metalsemiconductor transition in a 1T monolayer of MoS2. Phys. Rev. Lett. 112:157601.

50. Acerce, M., D. Voiry, and M. Chhowalla. 2015. Metallic 1t phase MoS2 nanosheets as supercapacitor electrode materials. Nat. Nanotechnol. 10:313–318.

51. Priyanka Ganguly, Moussab Harb, Zhen Cao, Luigi Cavallo, Ailish Breen, Saoirse Dervin, Dionysios D. Dionysiou, and Suresh C. Pillai,2D Nanomaterials for Photocatalytic Hydrogen Production,ACS Energy Letters 2019 4 (7), 1687-1709.

52. T.F. Jaramillo, K.P. Jørgensen, J. Bonde, J.H. Nielsen, S. Horch, I. Chorkendorff, Science 317 (2007) 100–102.

53. B. Hinnemann, P.G. Moses, J. Bonde, K.P. Jørgensen, J.H. Nielsen, S. Horch, I. Chorkendorff, J.K. Nørskov, J. Am. Chem. Soc. 127 (2005) 5308–5309.

54. J.B. Ding, Y. Zhou, Y.G. Li, S.J. Guo, X.Q. Huang, Chem. Mater. 28 (2016) 2074–2080.

55. J. Xie, J. Zhang, S. Li, F. Grote, X. Zhang, H. Zhang, R. Wang, Y. Lei, B. Pan, Y. Xie, J. Am. Chem. Soc. 135 (2013) 17881–17888.

56. Q.H. Wang, K. Kalantar-Zadeh, A. Kis, J.N. Coleman, M.S. Strano, Nat. Nanotechnol. 7 (2012) 699–712.

57. Q. Tang, D.E. Jiang, ACS Catal. 6 (2016) 4953–4961.

58. C.L. Tan, Z.M. Luo, A. Chaturvedi, Y.Q. Cai, Y.H. Du, Y. Gong, Y. Huang, Z.C. Lai, X. Zhang, L.R. Zheng, X.Y. Qi, M.H. Goh, J. Wang, S.K. Han, X.J. Wu, L. Gu, C. Kloc, H. Zhang, Adv. Mater. 30 (2018) 1705509.

59. Y. Yin, J.C. Han, Y.M. Zhang, X.H. Zhang, P. Xu, Q. Yuan, L. Samad, X.J. Wang, Y. Wang, Z.H. Zhang, P. Zhang, X.Z. Cao, B. Song, S. Jin, J. Am. Chem. Soc. 138 (2016) 7965–7972.

60. Zhipeng Liu, Lei Zhao, Yuhua Liu, Zhichao Gao, Shisheng Yuan, Xiaotian Li, Nan Li, Shiding Miao, Vertical nanosheet array of 1T phase MoS2 for efficient and stable hydrogen evolution, Applied Catalysis B: Environmental 246 (2019) 296–302.

61. K. Krishnamoorthy, G.K. Veerasubramani, S. Radhakrishnan, S.J. Kim, Supercapacitive properties of hydrothermally synthesized spheres like MoS2 nanostructures, Mater. Res. Bull. 50 (2014) 499–502.

62. N. Joseph, P.M. Shafi, A.C. Bose, Recent advances in 2D-MoS2 and its composite nanostructures for supercapacitor electrode application, Energy Fuel 34 (2020) 6558–6597.

63. S. Rani, M. Sharma, D. Verma, A. Ghanghass, R. Bhatia, I. Sameera, Two-dimensional transition metal dichalcogenides and their heterostructures: role of process parameters in top-down and bottom-up synthesis approaches, Mater. Sci.Semicond. Process. 139 (2022) 106313–106342.

64. J.B. Cook, H.-S. Kim, T.C. Lin, C.-H. Lai, B. Dunn, S.H. Tolbert, Pseudocapacitive charge storage in thick composite MoS2 nanocrystal-based electrodes, Adv. Energy Mater. 7 (2) (2016), 1601283.

65. B.A. Ali, O.I. Metwalli, A.S.G. Khalil, N.K. Allam, Unveiling the effect of the structure of carbon material on the charge storage mechanism in MoS2-based supercapacitors, ACS Omega 3 (11) (2018) 16301–16308.

66. S. Asaithambi, P. Sakthivel, M. Karuppaiah, K. Balamurugan, R. Yuvakkumar, M. Thambidurai, G. Ravi, Synthesis and characterization of various transition metals

doped SnO2@MoS2 composites for supercapacitor and photocatalytic applications, J. Alloys Compd. 853 (2021), 157060.

67. D. Sahoo, J. Shakya, S. Choudhury, S.S. Roy, L. Devi, B. Singh, S. Ghosh, B. Kaviraj, High-performance MnO2 nanowire/MoS2 nanosheet composite for a symmetrical solid-state supercapacitor, ACS Omega 7 (2022) 16895–16905.

68. X. Mao, Y. Zou, F. Xu, L. Sun, H. Chu, H. Zhang, J. Zhang, C. Xiang, Three-dimensional self-supporting Ti3C2 with MoS2 and Cu2O nanocrystals for high-performance flexible supercapacitors, ACS Appl. Mater. Interfaces 13 (2021) 22664–22675.

69. S. Wang, C. Qin, T. Feng, P. Zhao, K. Cheng, P. Zhou, Z. Li, Z. Lin, G. Liu, Enhanced supercapacitive performance of polyacrylonitrile derived hierarchical porous carbon via hybridizing with MoS2 nanosheets, J. Energy Storage 40 (2021) 102695–102704.

70. M. Saraf, K. Natarajan, S.M. Mobin, Emerging robust heterostructure of MoS2− rGO for high performance supercapacitors, ACS Appl. Mater. Interfaces 10 (2018) 16588–16595.

71. Sonam Rani, Manushree Tanwar, Meenu Sharma, Love Bansal, Rajesh Kumar, Ravi Bhatia, Sameera Ivaturi, Enhancing energy storage capabilities of MoS2 nanoflowers through designing nanoarchitecture by controlling synthesis growth parameters, Journal of Energy Storage 58 (2023) 106343.

72. Zhou Feng, Peipei Yang, Guosheng Wen, Haibo Li, Ying Liu, Xiuchen Zhao, One-step synthesis of MoS2 nanoparticles with different morphologies for electromagnetic wave absorption, Applied Surface Science 502 (2020) 144129.

73. B. Radisavljevic, A. Radenovic, J. Brivio, V. Giacometti, A. Kis, Single-layer MoS2 transistors, Nat. Nanotechnol. 6 (2011) 147–150.

74. W. Österle, A.I. Dmitriev, The role of solid lubricants for brake friction materials, Lubricants 4 (2016) 5.

75. N. Perea-Lopez, Z. Lin, N.R. Pradhan, A. Iniguez-Rabago, A.L. Elias, A. McCreary, et al., CVD-grown monolayered MoS2 as an effective photosensor operating at low-voltage, 2D Mater. 1 (2014) 011004.

76. K. Kam, B. Parkinson, Detailed photocurrent spectroscopy of the semiconducting group VIB transition metal dichalcogenides, J. Phys. Chem. 86 (1982) 463–467.

77. B. Liu, L. Chen, G. Liu, A.N. Abbas, M. Fathi, C. Zhou, High-performance chemical sensing using Schottky-contacted chemical vapor deposition grown monolayer MoS2 transistors, ACS Nano 8 (2014) 5304–5314.

78. Nahid Chaudhary, Manika Khanuja, Abid, S.S. Islam, Hydrothermal synthesis of MoS2 nanosheets for multiple wavelength optical sensing applications, Sensors and Actuators A 277 (2018) 190–198.

79. B. Radisavljevic, A. Radenovic, J. Brivio, V. Giacometti, A. Kis, Single-layer MoS2 transistors, Nat. Nanotechnol. 6 (2011) 147–150.

80. Y. Miki, D. Nakazato, H. Ikuta, T. Uchida, M. Wakihara, Amorphous MoS2 as the cathode of lithium secondary batteries, J. Power Sources 54 (1995) 508–510.

81. G. Eda, T. Fujita, H. Yamaguchi, D. Voiry, M. Chen, M. Chhowalla, Coherent atomic and electronic heterostructures of single-layer MoS2, ACS Nano 6 (2012) 7311–7317.

82. Z. Yin, H. Li, H. Li, L. Jiang, Y. Shi, Y. Sun, G. Lu, Q. Zhang, X. Chen, H. Zhang, Single-layer MoS2 phototransistors, ACS Nano 6 (2012) 74–80.

83. Z. Zeng, Z. Yin, X. Huang, H. Li, Q. He, G. Lu, F. Boey, H. Zhang, Single-layer semiconducting nanosheets: high-yield preparation and device fabrication, Angew. Chem. 123 (2011) 11289–11293.

84. H. Li, Z. Yin, Q. He, H. Li, X. Huang, G. Lu, D.W.H. Fam, A.I.Y. Tok, Q. Zhang,H. Zhang, Layered nanomaterials: fabrication of single-and multilayer MoS2 film-based field-effect transistors for sensing no at room temperature, Small 8 (2012)63–67.

85. K.K. Liu, W. Zhang, Y.H. Lee, Y.C. Lin, M.T. Chang, C.Y. Su, C.S. Chang, H. Li, Y. Shi, H. Zhang, Growth of large-area and highly crystalline MoS2 thin layers on insulating substrates, Nano Lett. 12 (2012) 1538–1544.

86. V. Varshney, S.S. Patnaik, C. Muratore, A.K. Roy, A.A. Voevodin, B.L. Farmer, MD simulations of molybdenum disulphide (MoS2): force-field parameterization and thermal transport behavior, Comp. Mater. Sci. 48 (2010) 101–108.

87. Y. Wang, G. Xing, Z.J. Han, Y. Shi, J.I. Wong, Z.X. Huang, K.K. Ostrikov, H.Y. Yang, Pre-lithiation of onion-like carbon/MoS2 nano-urchin anodes for high-performance rechargeable Lithium ion batteries, Nanoscale 6 (2014) 8884–8890.

88. J. Liu, Z. Zeng, X. Cao, G. Lu, L.H. Wang, Q.L. Fan, W. Huang, H. Zhang, Preparation of MoS2-polyvinylpyrrolidone nanocomposites for flexible nonvolatile rewritable memory devices with reduced graphene oxide electrodes, Small 8 (2012) 3517–3522.

89. Q. Jiang, X. Chen, L. Li, C. Feng, Z. Guo, Synthesis and electrochemical properties of molybdenum disulfide/carbon microsphere composite, J. Electron. Mater. 46 (2016) 1–9.

90. M. Choi, S.K. Koppala, D. Yoon, J. Hwang, S.M. Kim, J. Kim, A route to synthesis molybdenum disulfide-reduced graphene oxide (MoS2-RGO) composites using supercritical methanol and their enhanced electrochemical performance for Li-ion batteries, J. Power Sources 309 (2016) 202–211.

91. K. Chang, W. Chen, L. Ma, H. Li, H. Li, F. Huang, Z. Xu, Q. Zhang, J. Lee, Graphene-like MoS2/amorphous carbon composites with high capacity and excellent stability as anode materials for lithium ion batteries, J. Mater. Chem. 21 (2011) 6251–6257.

92. Y. Zhang, Y. Li, H. Li, F. Yin, Y. Zhao, Z. Bakenov, Synthesis of hierarchical MoS2 microspheres composed of nanosheets assembled via facile hydrothermal method as anode material for lithium-ion batteries, J. Nanopart. Res. 18 (2016) 1–9.

93. N. Lingappan, N.H. Van, S. Lee, D.J. Kang, Growth of three-dimensional flower-like molybdenum disulfide hierarchical structures on graphene/carbon nanotube network: an advanced heterostructure for energy storage devices, J. Power Sources 280(2015) 39–46.

94. Xiaodi Zheng, Yanli Zhu, Yalun Sun, Qingjie Jiao, Hydrothermal synthesis of MoS2 with different morphology and its performance in thermal battery, Journal of Power Sources 395 (2018) 318–327.

95. Sharma M, Mohapatra P K and Bahadur D 2017 Front. Mater. Sci. 11 366.

96. Zhu S and Wang D 2017 Adv. Energy Mater. 7 1700841.

97. Vattikuti S V P and Byon C 2016 Superlattices Microstruct.100 514.

98. Mishra A K, Lakshmi K V and Huang L 2015 Sci. Rep. 5 15718.

99. Quinn M D J, Ho N H and Notley S M 2013 ACS Appl.Mater. Interfaces 5 12751.

100. Johari P and Shenoy V B 2012 ACS Nano 6 5449.

101. Anjali Rani, Kulvinder Singh, Prianka Sharma, Investigation of visible light photocatalytic degradation of organic dyes by MoS2 nanosheets synthesized by different routes, Bull. Mater. Sci. (2022) 45:63.

102. Kibsgaard J, Chen Z, Reinecke BN, Jaramillo TF. Engineering the surface structure of MoS2 to preferentially expose active edge sites for electrocatalysis. Nat Mater 2012;11:963e9.

103. Zhang L, Wu HB, Yan Y, Wang X, Lou XW (David). Hierarchical MoS2 microboxes constructed by nanosheets with enhanced electrochemical properties for lithium storage and water splitting. Energy Environ Sci 2014;7:3302e6.

104. Karunadasa HI, Montalvo E, Sun YJ, Majda M, Long JR, Chang CJ. A molecular MoS2 edge site mimic for catalytic hydrogen generation. Science 2012;335:698e702.

105. Xia BY, Yan Y, Wang X, Lou XW (David). Recent progress on graphene-based hybrid electrocatalysts. Mater Horiz 2014;1:379e99.

106. Bian XJ, Zhu J, Liao L, Scanlon MD, Ge PY, Ji C, et al. Nanocomposite of MoS2 on ordered mesoporous carbon nanospheres: a highly active catalyst for electrochemical hydrogen evolution. Electrochem Commun 2012;22:128e32.

107. Chang K, Chen WX. L-cysteine-assisted synthesis of layered MoS2/graphene composites with excellent electrochemical performances for lithium ion batteries. ACS Nano 2011;5:4720e8.

108. Albu-Yaron A, Levy M, Tenne R, Popovitz-Biro R, Weidenbach M, Bar-Sadan M, et al. MoS2 hybrid nanostructures: from octahedral to quasi-spherical shells within individual nanoparticles. Angew Chem Int Ed 2011;50:1810e4.

109. Li H, Yin ZY, He QY, Li H, Huang X, Lu G, et al. Fabrication of single- and multilayer MoS2 film-based field-effect transistors for sensing NO at room temperature. Small 2012;8:63e7.

110. Ambrosi A, Chia XY, Sofer Z, Pumera M. Enhancement of electrochemical and catalytic properties of MoS2 through ball-milling. Electrochem Commun 2015;54:36e40.

111. Matte HSSR, Gomathi A, Manna AK, Late DJ, Datta R, Pati SK, et al. MoS2 and WS2 analogues of graphene. Angew Chem Int Ed 2010;49:4059e62.

112. Zhou KG, Mao NN, Wang HX, Peng Y, Zhang HL. A mixedsolvent strategy for efficient exfoliation of inorganic graphene analogues. Angew Chem Int Ed 2011;50:10839e42.

113. Altavilla C, Sarno M, Ciambelli P. A novel wet chemistry approach for the synthesis of hybrid 2D free-floating single or multilayer nanosheets of MS2@oleylamine (M¼Mo, W). Chem Mater 2011;23:3879e85.

114. Deng J, Yuan WT, Ren PJ, Wang Y, Deng DH, Zhang Z, et al. High-performance hydrogen evolution electrocatalysis by layer-controlled MoS2 nanosheets. RSC Adv 2014;4:34733e8.

115. Wen-Hui Hu, Guan-Qun Han, Fang-Na Dai, Yan-Ru Liu, Xiao Shang, Bin Dong, Yong-Ming Chai, Yun-Qi Liu, Chen-Guang Liu, Effect of pH on the growth of MoS2 (002) plane and electrocatalytic activity for HER, International Journal of Hydrogen Energy 41 (2016) 294-299.

116. Daryani M, Simchi A, Sadati M, Hosseini MH, Targholizadeh H, Khakbiz M. Effects of Ti-based catalysts on hydrogen desorption kinetics of nanostructured magnesium hydride. Int J Hydrogen Energy. 2014;39(36):21007-21014.

117. Lu X, Lin Y, Dong H. One-step hydrothermal fabrication of three-dimensional MoS2 nanoflower using polypyrrole as template for efficient hydrogen evolution reaction. Sci Rep. 2017;7(1):42309.

118. Radecka RM, Trenczek M. Importance of the band gap energy and flat band potential for application of modified TiO2 photoanodes in water photolysis. J Power Sources. 2008;181(1):46-55.

119. Wang M, Ren F, Zhou J. N doping to ZnO nanorods for photoelectrochemical water splitting under visible light: engineered impurity distribution and terraced band structure. Sci Rep. 2015;5(1):12925.

120. Sivula DR, Formal FL, Gratzel A. Solar water splitting: progress using hematite (α-Fe2O3) photoelectrodes. ChemSusChem. 2011;4(4):432-449.

121. WooKim T, Choi KS. Nanoporous BiVO4 photoanodes with dual-layer oxygen evolution catalysts for solar water splitting. Science. 2014;1245026.

122. Neto AH, Guinea F, Peres NMR. The electronic properties of graphene. Rev Mod Phys. 2009;81(1):109-162.

123. Jain P, Chhagan L, Ankur J. Hydrogen storage in Mg: A most promisingmaterial.Int J Hydrogen Energy. 2010;35(10):5133-5144.

124. Late DJ, Rout CS, Chakravarty D. Emerging energy applications of two-dimensional layered materials. Can Chem Trans. 2015;3:118-157.

125. Matte HSS, Gomathi A, Manna AK. MoS2 and WS2 analogues of graphene. Angew Chem Int Ed. 2010;49(24):4059-4062.

126. Radisavljevic B, Radenovic A, Brivio J. Single-layer MoS2 transistors. Nat Nanotechnol. 2011;6(3):147-150.

127. Li Y, Wang H, Xie L. MoS2 nanoparticles grown on graphene: an advanced catalyst for the hydrogen evolution reaction. J Am Chem Soc. 2011;133(19):7296-7299.

128. Chang K, Mei Z, Wang T. MoS2/graphene cocatalyst for efficient photocatalytic H2 evolution under visible light irradiation. ACS Nano. 2014;8(7):7078-7087.

129. Khalid Nadeem Riaz, Nadeem Yousaf, Muhammad Bilal Tahir, Zainab Israr, Tahir Iqbal, Facile hydrothermal synthesis of 3D flower-like La-MoS2 nanostructure for photocatalytic hydrogen energy production, DOI: 10.1002/er.4286.

130. Lijun Luo, Miao Shi, Shimin Zhao, Wei Tan, Xi Lin, Hongbin Wang, Fengzhi Jiang, Hydrothermal synthesis of MoS2 with controllable morphologies and its adsorption properties for bisphenol A, Journal of Saudi Chemical Society (2019) 23, 762–773.

131. Solomon, G.; Mazzaro, R.; You, S.; Natile, M.M.; Morandi, V.; Concina, I.; Vomiero, A. Ag2S/MoS2 Nanocomposites Anchored on Reduced Graphene Oxide: Fast Interfacial Charge Transfer for Hydrogen Evolution Reaction. ACS Appl. Mater. Interfaces 2019, 11, 22380–22389.

132. B. Cho, J. Yoon, S.K. Lim, A.R. Kim, D.-H. Kim, S.-G. Park, J.-D. Kwon, Y.-J. Lee, K.-H. Lee, B.H. Lee, H.C. Ko, M.G. Hahm, Chemical sensing of 2D graphene/MoS_2 heterostructure device, ACS appl, Mater. Interfaces 7 (2015) 16775–16780.

133. J. Meng, H.-D. Song, C.-Z. Li, Y. Jin, L. Tang, D. Liu, Z.-M. Liao, Lateral graphene p–n junctions formed by the graphene/MoS_2 hybrid interface, Nanoscale 7 (2015) 11611–11619.

134. Park SY, Lee JE, Kim YH, Kim JJ, Shim YS, Kim SY, Lee MH, Jang HW. Room temperature humidity sensors based on rGO/MoS_2 hybrid composites synthesized by hydrothermal method. Sensors and Actuators B: Chemical. 2018 Apr 1;258: 775-82.

135. F. Huang, A. Yan, Y. Sui, F. Wei, J. Qi, Q. Meng, One-step hydrothermal synthesis of Ni_3S_4@MoS_2 nanosheet on carbon fiber paper as a binder-free anode for supercapacitor, J. Mater. Sci. Mater. Electron. 28 (2017) 12747e12754.

136. L. Cao, S. Yang, W. Gao, Direct laser-patterned micro-supercapacitors from paintable MoS_2 films, Small 9 (2013) 2905.

137. Huang, F., Meng, R., Sui, Y., Wei, F., Qi, J., Meng, Q. and He, Y., 2018. One-step hydrothermal synthesis of a CoS_2@ MoS_2 nanocomposite for high-performance supercapacitors. *Journal of Alloys and Compounds*, *742*, pp.844-851.

138. K. Peng, L. Fu, J. Ouyang, H. Yang, Adv. Funct. Mater. 26 (2016) 2666–2675.

139. Chen, P., Zeng, S., Zhao, Y., Kang, S., Zhang, T. and Song, S., 2020. Synthesis of unique-morphological hollow microspheres of MoS_2@ montmorillonite nanosheets for the enhancement of photocatalytic activity and cycle stability. *Journal of Materials Science & Technology*, *41*, pp.88-97.

140. Vasudevan, Mugashini, et al. "Facile synthesis of MoS_2 nanoflower-Ag NPs grown on lignin-derived graphene for Troponin I aptasensing." *Chemical Engineering Journal* 468 (2023): 143613.

141. Zou, Leideng, et al. "MoS_2/RGO hybrids prepared by a hydrothermal route as a highly efficient catalytic for sonocatalytic degradation of methylene blue." *Results in Physics* 14 (2019): 102458.

142. Xu T, Zhou S, Tao H, Wang W, Zhang K. 2019. Influence of Ag on photocatalytic performance of Ag/ZnO nanosheet photocatalystsag. J Cent South Univ. 26(7):2011-2018.

143. Li, Jie. "Clean energy of $NiCo_2O_4/MoS_2$ nanocomposites prepared by hydrothermal method." *Journal of Biotech Research* 15 (2023): 1-11.

144. Song, Haishen, et al. "Hydrothermal synthesis and electrochemical properties of MoS_2/C nanocomposite." *International Journal of Electrochemical Science* 13.7 (2018): 6708-6716.

145. Kaushik, Arvind, et al. "MoS_2–Ag nanocomposite-based SERS substrates with an ultralow detection limit." *ACS Applied Nano Materials* 6.11 (2023): 9236-9246.

146. Vasudevan, Mugashini, et al. "Characterizations of synthesized laser scribed graphene/molybdenum disulfide (LSG/MoS_2) hybrids for supercapacitor performance." *Journal of Water and Environmental Nanotechnology* 8.2 (2023): 137-150.

147. Ma, Guansheng, et al. "Hydrothermal synthesis of MoS_2/SnS_2 photocatalysts with heterogeneous structures enhances photocatalytic activity." *Materials* 16.12 (2023): 4436.

148. Askari, Mohammad Bagher, et al. "Fe_3O_4@ MoS_2/RGO as an effective nano-electrocatalyst toward electrochemical hydrogen evolution reaction and methanol oxidation in two settings for fuel cell application." *Journal of colloid and interface science* 537 (2019): 186-196.

149. D. Chiappe, E. Scalise, E. Cinquanta, C. Grazianetti, B. Van Den Broek, M. Fanciulli, M. Houssa, A. Molle, Two-dimensional Si nanosheets with local hexagonal structure on a MoS2 surface, Adv. Mater. 26 (2014) 2096–2101.

150. Prateek Sharma, Mrityunjay Kumar Singh, Mohan Singh Mehata, Sunlight-driven MoS2 nanosheets mediated degradation of dye (crystal violet) for wastewater treatment, Journal of Molecular Structure 1249 (2022) 131651.

151. Gauthaman Chandrabose, Avishek Dey, Shivani Singh Gaur, Sudhagar Pitchaimuthu, Hema Jagadeesan, N. St John Braithwaite, Vimalnath Selvaraj, Vasant Kumar, Satheesh Krishnamurthy, Removal and degradation of mixed dye pollutants by

integrated adsorption-photocatalysis technique using 2-D MoS2/TiO2 nanocomposite, Chemosphere 279 (2021) 130467.

152. Yunpeng Liu, Yuhang Li, Feng Peng, Yuan Lin, Siyuan Yang, Shengsen Zhang, Hongjuan Wang, Yonghai Cao, Hao Yu, 2H- and 1T- mixed phase few-layer MoS2 as a superior to Pt co-catalyst coated on TiO2 nanorod arrays for photocatalytic hydrogen evolution, Applied Catalysis B: Environmental, 241,236-245.

153. F. Han, V.S. Rao Kambala, M. Srinivasan, D. Rajarathnam, R. Naidu, Appl. Catal. A Gen. 359 (2009) 25

154. J. Theerthagiri, R.A. Senthil, B. Senthilkumar, A.R. Polu, J. Madhavan, M. Ashokkumar, J. Solid State Chem. 252 (2017) 43.

155. Y. Gao, C. Chen, X. Tan, H. Xu, K. Zhu, J. Colloid Interface Sci. 476 (2016) 62.

156. Joy Sankar Roy, Gabriel Dugas, Steeve Morency, Younes Messaddeq, Rapid degradation of Rhodamine B using enhanced photocatalytic activity of MoS2 nanoflowers under concentrated sunlight irradiation, Physica E 120 (2020) 114114.

157. Dhanesh Gawari, Vikram Pandit, Niteen Jawale, Pramod Kamble, Layered MoS2 for photocatalytic dye degradation, Materials Today: Proceedings 53 (2022) 10–14.

158. J. H. Appel, D. O. Li, J. D. Podlevsky, A. Debnath, A. A. Green, Q. H. Wang, and J. Chae, “Low Cytotoxicity and Genotoxicity of Two-Dimensional MoS2 and WS2,” ACS Biomaterials Science & Engineering, 2, pp. 361−367, 2016.

159. Debabrat Kalita, Lakhi Chetia and Gazi A, Photocatalytic Degradation of Methyl Orange using MoS2 nanoparticles as catalyst, AhmedADBU-Journal of Engineering Technology, Volume 7, Issue 2, December 2018.

160. S. V. P. Vattikuti, C. Byon and C. V. Reddy, Superlattices Microstruct., 2015, 85, 124–132.

161. W. Zhou, Z. Yin, Y. Du, X. Huang, Z. Zeng, Z. Fan, H. Liu, J. Wang and H. Zhang, Small, 2013, 9, 140–147.

162. H. K. Sadhanala, Subrata Senapati, Krishna Villa Harika, Karuna Kar Nanda, Aharon Gedanken, Green synthesis of MoS2 nanoflowers for efficient degradation of

methylene blue and crystal violet dyes under natural sunlight conditions, New J. Chem., 2018, 42, 14318.

163. Peng Y, Meng Z, Zhong C, Lu J, Yu W, Jia Y B et al 2001 Chem. Lett. 30 772.

164. ANJALI RANI, KULVINDER SINGH, PRIANKA SHARMA, Investigation of visible light photocatalytic degradation of organic dyes by MoS2 nanosheets synthesized by different routes, Bull. Mater. Sci. (2022) 45:63.

165. Karthigaimuthu Dharamalingam, B. Arjun Kumar, G. Ramalingam, S. Sasi Florence, Kumar Raju, P. Senthil Kumar, Saravanan Govindaraju, Elangovan Thangavel, The role of sodium dodecyl sulfate mediated hydrothermal synthesis of MoS2 nanosheets for photocatalytic dye degradation and dye-sensitized solar cell application, Chemosphere 294 (2022) 133725.